

---

**Research Article: New Research | Sensory and Motor Systems**

**Afferent Fiber Remodeling in the Somatosensory Thalamus of Mice as a Neural Basis of Somatotopic Reorganization in the Brain and Ectopic Mechanical Hypersensitivity after Peripheral Sensory Nerve Injury**

Thalamic Remodeling for Ectopic sensations

Yuichi Takeuchi<sup>1</sup>, Hironobu Osaki<sup>1</sup>, Yuki Yagasaki<sup>1,2</sup>, Yoko Katayama<sup>1</sup> and Mariko Miyata<sup>1</sup>

<sup>1</sup>Department of Physiology School of Medicine, Tokyo Women's Medical University, 8-1 Kawada-Cho, Shinjuku, Tokyo Japan Ku, 162-8666

<sup>2</sup>Division of Women Health Care Professionals and Researchers Support, TWUM Career Development Center for Medical Professionals, Tokyo Women's Medical University, 8-1 Kawada-Cho, Shinjuku, Tokyo Japan Ku, 162-8666

DOI: 10.1523/ENEURO.0345-16.2017

Received: 21 November 2016

Revised: 22 February 2017

Accepted: 3 March 2017

Published: 23 March 2017

---

**Author Contributions:** YT and MM Designed research; YT, HO, YY, and YK Performed research; YT, HO, YY, and YK Analyzed data; YT and MM Wrote the paper.

**Conflict of Interest:** Authors report no conflict of interest.

**Correspondence should be addressed to:** Mariko Miyata, MD, PhD; Department of Physiology, School of Medicine, Tokyo Women's Medical University, 8-1 Kawada-cho, Shinjuku-ku, Tokyo 162-8666, Japan; Tel. and Fax.: +81-3-5269-7413; E-mail: [mmiyata@twmu.ac.jp](mailto:mmiyata@twmu.ac.jp)

**Cite as:** eNeuro 2017; 10.1523/ENEURO.0345-16.2017

**Alerts:** Sign up at [eneuro.org/alerts](http://eneuro.org/alerts) to receive customized email alerts when the fully formatted version of this article is published.

Accepted manuscripts are peer-reviewed but have not been through the copyediting, formatting, or proofreading process.

This is an open-access article distributed under the terms of the Creative Commons Attribution 4.0 International (<http://creativecommons.org/licenses/by/4.0>), which permits unrestricted use, distribution and reproduction in any medium provided that the original work is properly attributed.

Copyright © 2017 the authors

1 Submitted to *eNeuro*

2 Research Article (New Research, Sensory and Motor System)

3 **Title page**

- 4 **1. Manuscript Title:** Afferent fiber remodeling in the somatosensory thalamus of mice as a  
5 neural basis of somatotopic reorganization in the brain and ectopic mechanical  
6 hypersensitivity after peripheral sensory nerve injury
- 7 **2. Abbreviated Title:** Thalamic Remodeling for Ectopic sensations
- 8 **3. Authors and Affiliations:** Yuichi Takeuchi<sup>1</sup>, Hironobu Osaki<sup>1</sup>, Yuki Yagasaki<sup>1,2</sup>, Yoko  
9 Katayama<sup>1</sup>, and Mariko Miyata<sup>1</sup>; <sup>1</sup>Department of Physiology, School of Medicine, Tokyo  
10 Women's Medical University, 8-1 Kawada-cho, Shinjuku-ku, Tokyo 162-8666, Japan;  
11 <sup>2</sup>Division of Women Health Care Professionals and Researchers Support, TWUM Career  
12 Development Center for Medical Professionals, Tokyo Women's Medical University, 8-1  
13 Kawada-cho, Shinjuku-ku, Tokyo 162-8666, Japan
- 14 **4. Author Contributions:** YT and MM Designed research; YT, HO, YY, and YK  
15 Performed research; YT, HO, YY, and YK Analyzed data; YT and MM Wrote the paper.
- 16 **5. Correspondence should be addressed to:** Mariko Miyata, MD, PhD; Department of  
17 Physiology, School of Medicine, Tokyo Women's Medical University, 8-1 Kawada-cho,  
18 Shinjuku-ku, Tokyo 162-8666, Japan; Tel. and Fax.: +81-3-5269-7413; E-mail:  
19 [mmiyata@twmu.ac.jp](mailto:mmiyata@twmu.ac.jp)
- 20 **6. Number of Figures:** 8
- 21 **7. Number of Tables:** 3
- 22 **8. Number of Multimedia:** 0
- 23 **9. Number of words for Abstract:** 245
- 24 **10. Number of words for Significance Statement:** 105
- 25 **11. Number of words for Introduction:** 642
- 26 **12. Number of words for Discussion:** 1510
- 27 **13. Acknowledgements:** We thank E. Naraba, and M. Hatakenaka for technical assistance,  
28 Drs. F. M. Rijli and T. Iwasato for the gift of *Krox-20<sup>Cre</sup>* and *Hoxa2-cre* mice, Drs. M.  
29 Watanabe and M. Yamasaki for technical suggestions, Dr. Y. Honda for support with the  
30 NeuroLucida system, and Dr. G. Miyoshi for comments on our manuscript.
- 31 **14. Conflict of Interest:** Authors report no conflict of interest.
- 32 **15. Funding sources:** This study was supported by Grants-in-Aid for Scientific Research  
33 (18500316, 20021029, 22800063, 23500400, 25870757, 26290010, 09J00032, 15K21387),  
34 Grant-in-Aid for Scientific Research on Innovative Areas (15H01667, 16H01344), The  
35 Uehara Memorial Foundation, Aya Irisawa Memorial Promotion Award, SHISEIKAI  
36 Scholarship Fund for basic researcher of medical science, Keiko Watanabe Award, and  
37 Research grant for Support Center for Women Health Care Professionals and Researchers,  
38 Tokyo Women's Medical University.

39

40 **Abstract**

41 Plastic changes in the central nervous system in response to peripheral sensory nerve injury  
42 are a series of complex processes, ranging from local circuit remodeling to somatotopic  
43 reorganization. However, the link between circuit remodeling and somatotopic reorganization  
44 remains unclear. We have previously reported that transection of the primary whisker sensory  
45 nerve causes the abnormal rewiring of lemniscal fibers (sensory afferents) on a neuron in the  
46 mouse whisker sensory thalamus (V2 VPM). In the present study, using transgenic mice  
47 whose lemniscal fibers originate from the whisker sensory principle trigeminal nucleus  
48 (PrV2) are specifically labeled, we identified that the transection induced retraction of PrV2-  
49 originating lemniscal fibers and invasion of those not originating from PrV2 in the V2 VPM.  
50 This anatomical remodeling with somatotopic reorganization was highly correlated with the  
51 rewiring of lemniscal fibers. Origins of the non-PrV2-origin lemniscal fibers in the V2 VPM  
52 included the mandibular subregion of trigeminal nuclei and the dorsal column nuclei, which  
53 normally represent body parts other than whiskers. The transection also resulted in ectopic  
54 receptive fields of V2 VPM neurons and extraterritorial pain behavior on the uninjured  
55 mandibular region of the face. The anatomical remodeling, emergence of ectopic receptive  
56 fields, and extraterritorial pain behavior all concomitantly developed within a week and lasted  
57 more than three months after the transection. Our findings, thus, indicate a strong linkage  
58 between these plastic changes after peripheral sensory nerve injury, which may provide a  
59 neural circuit basis underlying large-scale reorganization of somatotopic representation and  
60 abnormal ectopic sensations.

61 **Significance Statement**

62 Peripheral sensory nerve injury causes various plastic changes in the somatosensory pathway.  
63 However, the link between these plastic changes remains poorly understood. In the present  
64 study, taking advantage of a transgenic mouse line, whose somatotopic information on  
65 afferent fibers is specifically visualized, we identified that afferent fiber remodeling in the  
66 thalamus after sensory nerve injury mediates large-scale somatotopic reorganization. Since  
67 the afferent fiber remodeling in the thalamus concomitantly occurred and lasted along with  
68 reorganization of somatotopic representation in the thalamus and ectopic pain behavior, the  
69 afferent fiber remodeling with somatotopic reorganization in the thalamus could potentially be  
70 a neural basis of clinically problematic ectopic sensations.

71

**72 Introduction**

73 Neural circuitry in the central nervous system (CNS) is capable of remodeling in response to  
74 peripheral sensory nerve injury (Woolf and Mannion, 1999; Navarro *et al.*, 2007; Kaas *et al.*,  
75 2008). At the neural circuit level, peripheral sensory nerve injury such as afferent fiber  
76 transection and ligation causes anatomical remodeling of presynaptic axon fibers throughout  
77 the sensory afferent pathway from the spinal cord to the cortex (Darian-Smith and Gilbert,  
78 1994; Sengelaub *et al.*, 1997; Florence *et al.*, 1998; Jain *et al.*, 2000; Okamoto *et al.*, 2001;  
79 Graziano and Jones, 2009; Yamahachi *et al.*, 2009). Peripheral sensory nerve injury also  
80 induces rapid remodeling of postsynaptic dendritic spines (Kim and Nabekura, 2011).  
81 Moreover, the efficacy of functional synaptic transmission is altered after injury at all levels  
82 along the afferent axis (Kohno *et al.*, 2003; Takeuchi *et al.*, 2012; Yu *et al.*, 2012). From a  
83 systems perspective, peripheral sensory nerve injury causes reorganization of somatotopic  
84 representation of the brain, such as changes in size of receptive fields in the somatosensory  
85 axis in anesthetized animals (Merzenich *et al.*, 1984; Waite, 1984; Garraghty and Kaas, 1991).  
86 Such reorganization of receptive fields can be large in scale and extends beyond the  
87 somatotopic border (Pons *et al.*, 1991; Jones and Pons, 1998). Furthermore, peripheral sensory  
88 nerve injury also induces abnormal ectopic sensations in humans such as extraterritorial  
89 orofacial pain (Kobayashi *et al.*, 2011; Renton *et al.*, 2012; Tseng *et al.*, 2012; Okada-Ogawa  
90 *et al.*, 2015) and phantom referred sensation (e.g., hand sensations evoked by face touch),  
91 which occasionally results in pain (Ramachandran and Hirstein, 1998; Flor *et al.*, 2006).  
92 Large-scale somatotopic reorganization also correlates with phantom pain sensation,  
93 suggesting a possible causal relationship (Flor *et al.*, 1995; Grüsser *et al.*, 2001). However,  
94 while there are scattered pieces of evidence from the neural circuit level to the systems level,  
95 the linkage between particular neural circuitry remodeling and the somatotopic reorganization  
96 that would ultimately lead to abnormal ectopic sensation remains unclear. This is mainly

97 because the somatotopic information that remodeled axon fibers carry has not been fully  
98 identified.

99         The somatosensory thalamus receives lemniscal fibers (sensory afferents) from the  
100 brain stem and projects to the primary somatosensory cortex (Watson *et al.*, 2012).  
101 Connections between lemniscal fibers and thalamic neurons in the whisker sensory thalamus  
102 (V2 VPM) of the mouse have been a representative model of functional circuit remodeling  
103 such as developmental synapse elimination (Arsenault and Zhang, 2006); innervation of a  
104 single lemniscal fiber to a mature V2 VPM neuron is completed via developmental synapse  
105 elimination (Arsenault and Zhang, 2006; Takeuchi *et al.*, 2014). We have previously  
106 demonstrated that complete transection of the primary whisker sensory nerve of mice causes  
107 robust abnormal rewiring of lemniscal fibers, in that multiple lemniscal fibers are newly  
108 recruited onto a V2 VPM neuron (IONC model) (Takeuchi *et al.*, 2012). Together with  
109 evidence accumulated in *in vivo* studies, we hypothesized that newly recruited lemniscal  
110 fibers originate from different sources, other than the whisker sensory principle trigeminal  
111 nucleus (PrV2), which leads to somatotopic reorganization and finally abnormal ectopic  
112 sensations.

113         In the present study, taking advantage of the IONC model and Krox20-Ai14—a  
114 transgenic mouse line, whose PrV2-origin lemniscal fibers are specifically visualized—, we  
115 confirmed that newly recruited lemniscal fibers found in the IONC model originated specific  
116 brain stem nuclei, which normally represent the mandibular (V3) region of the face and/or  
117 other body parts. We also observed ectopic receptive fields of V2 VPM neurons and  
118 extraterritorial mechanical hypersensitivity in the corresponding V3 region. Furthermore, all  
119 these plastic changes emerged and lasted over a similar time course. Our results, thus, indicate  
120 that there is a close link between neural circuitry remodeling with somatotopic reorganization  
121 and ectopic sensations. We propose that the afferent remodeling in the thalamus after

Takeuchi *et al.*, 2017

- 122 peripheral sensory nerve injury may serve as a neural basis for abnormal ectopic sensations  
123 such as extraterritorial orofacial pain and phantom referred sensation.

**124 Materials and Methods****125 Animals**

126 All experiments were approved by the Animal Care and Use Committee of the Tokyo  
127 Women's Medical University and performed according to the institutional guidelines. To  
128 visualize the PrV2-origin lemniscal fibers, *Krox-20<sup>cre</sup>* mice (RRID:IMSR\_JAX:025744)  
129 (Voiculescu et al., 2000) and Cre-dependent tdTomato reporter mice  
130 (RRID:IMSR\_JAX:007914) (Madisen et al., 2010) were crossed, and the Cre-positive pups  
131 (Krox20-Ai14 mice) were used as previously described (Takeuchi et al., 2014). Wild-type  
132 C57BL/6 mice (RRID:IMSR\_JAX:000664) were purchased from SLC. Mice were fed a  
133 commercial diet and water *ad libitum* with controlled temperature, humidity, and lighting (12  
134 h light/dark cycle). Both sexes of P21–adult mice were used. Numbers of mice used were 120  
135 Krox20-Ai14 and 186 wild-type.

136

**137 Genotyping**

138 *Krox-20<sup>cre</sup>* mice were genotyped by a standard PCR procedure, using the following primers:  
139 CW-Cre2, 5'-ACC TGA TGG ACA TGT TCA GGG ATC G-3' and CW-Cre3, 5'-TCC GGT  
140 TAT TCA ACT TGC ACC ATG C-3', producing a 108-bp fragment from the *cre* allele  
141 (Iwasato et al., 2004). Krox20-Ai14 pups were genotyped by PCR and/or detecting tdTomato  
142 signals in vibrissal follicles expressed from late pregnancy (Voiculescu et al., 2000). Results  
143 of both typing methods were always consistent.

144

**145 Infraorbital nerve cut (IONC)**

146 The primary whisker sensory nerve (infraorbital nerve: ION) of the left side was exposed and  
147 completely transected under ketamine/xylazine anesthesia (80/10 mg/kg, i.p.) as previously  
148 described (Takeuchi et al., 2012). The cut was conducted on P21 or in two-months old mice.

149 For long survival case after the cut, the ION was tightly ligated by 6-0 silken thread before cut,  
150 and a plate of ethylene-vinyl acetate copolymer was placed between stumps to prevent nerve  
151 regeneration (Kakizawa *et al.*, 2005).

152

### 153 **Whisker deprivation**

154 All mystacial vibrissae on the left side of the snout were deprived every other day from P21 to  
155 the perfusion day ranging from P28 to P32. Under a dissecting microscope, vibrissae of  
156 isoflurane-anesthetized mice were carefully plucked out using fine tweezers by applying slow  
157 and steady tension to the base of the vibrissa until the vibrissa slipped out of the follicle  
158 (Arsenault and Zhang, 2006).

159

### 160 **Histology**

#### 161 *Perfusion and Cryosectioning*

162 Mice were deeply anesthetized with pentobarbital (i.p.) and transcardially perfused with ice-  
163 cold saline followed by 4% paraformaldehyde (PFA) and 0.2% picric acid in 0.1 M phosphate  
164 buffer (PB) (pH 7.2–7.3). After removal, brains were postfixed overnight, infiltrated with  
165 sucrose gradient, blocked, and frozen on dry ice. Thalamic or brain stem sections (20  $\mu$ m  
166 thickness, coronal or horizontal plane) were made using a freezing microtome. Sections were  
167 collected in antifreeze solution, rinsed in 0.1 M phosphate buffered saline (PBS), and then  
168 subjected to one of the staining procedures described below. All staining procedures were  
169 performed at room temperature unless otherwise noted. For series of quantitative fluorescence  
170 measurements (tdTomato fluorescence measurements, VGluT2 and VGluT2-MAP2  
171 immunohistochemistry), eight consecutive horizontal sections, total 160  $\mu$ m-thick, centered at  
172 the cloud of the tdTomato-labeled PrV2-origin lemniscal fiber terminals in the V2 VPM were  
173 collected from each Krox20-Ai14 mouse. Four alternating sections of them were used for

174 fluorescent staining and measurements. The remaining four sections were subjected to  
175 cytochrome oxidase (CO) staining (Takeuchi *et al.*, 2014).

176

177 *Fluorescent Nissl counter-staining of cryosections*

178 Sections were first mounted on glass slides. Sections were then incubated with PBS  
179 containing 0.3% Triton X-100 (PBS-X) for 10 min, washed with PBS, incubated with a  
180 fluoro-Nissl solution (N-21479 or N-21480; Thermo Fisher Scientific) for 40 min, washed  
181 with PBS, incubated with PBS-X for 10 min, and washed with PBS again. Sections were  
182 finally cover-slipped with 50% glycerol and 2.5% triethylene diamine in PBS.

183

184 *VGluT2 immunohistochemistry*

185 All incubations were followed by washing with PBS-X. Sections were incubated successively  
186 with 10% normal goat serum (NGS) in PBS-X for 30 min, 1  $\mu$ g/ml guinea pig anti-vesicular  
187 glutamate transporter type 2 (VGluT2) polyclonal antibody (Frontier Institute Cat# VGluT2-  
188 GP, RRID:AB\_2571621) (Miyazaki *et al.*, 2003) in PBS-X containing 1% NGS and 0.02%  
189 sodium azide (PBS-XG) overnight, and Alexa Fluor 633-conjugated goat anti-guinea pig IgG  
190 (A-21105; Thermo Fisher Scientific) for 2 h. Sections were then mounted, counterstained, and  
191 cover-slipped.

192

193 *MAP2 and VGluT2 double immunohistochemistry*

194 To examine contacts between V2 VPM neurons and lemniscal fiber terminals, they were  
195 simultaneously labeled with MAP2 and VGluT2, respectively. Sections were incubated  
196 successively with 10% normal donkey serum (NDS) in PBS-X for 30 min, a mixture of 1<sup>st</sup>  
197 antibodies (Frontier Institute Cat# MAP2-Go, RRID:AB\_2571793 and Frontier Institute Cat#  
198 VGluT2-Rb, RRID:AB\_2571619, 1  $\mu$ g/ml for each) in PBS containing 1% NDS and 0.02%

199 sodium azide (PBS-XD) (Miura et al., 2006) overnight, and a mixture of 2<sup>nd</sup> antibodies (Alexa  
200 Fluor 647-conjugated donkey anti-goat IgG: A-21447 and Alexa Fluor 488-conjugated  
201 donkey anti-rabbit IgG: A-21206; Thermo Fisher Scientific) for 2 h. Sections were then  
202 mounted, counterstained, and cover-slipped.

203

#### 204 *Anterograde labeling of the PrV2-origin lemniscal fibers*

205 Four days after IONC, mice were anesthetized with a ketamine/xylazine cocktail (80/10  
206 mg/kg, i.p.) and then mounted on a stereotaxic apparatus. An anterograde tracer, 2%  
207 biotinylated dextran amine (BDA) (Thermo Fisher Scientific Cat# D1956,  
208 RRID:AB\_2307337) was filled in a glass electrode (impedance: 1–5 M $\Omega$ ; tip 10–20  $\mu$ m). To  
209 inject BDA in the PrV2, the electrode was inserted 25°–obliquely from the left occipital  
210 cortex (coordinates in mm: 1.75–1.80 posterior and 1.70–1.75 lateral from the bregma) and  
211 then caudally advanced 5.70–5.90 mm (Franklin and Paxinos, 2008). To precisely locate the  
212 electrode in the PrV2, we monitored neural firing extracellularly along the track in response to  
213 tactile stimuli on the face with amplifiers (MEZ-8300 and AVH-11; Nihon Kohden). In the  
214 PrV2, BDA was iontophoretically ejected as anodal currents (+1–5  $\mu$ A, 3 s on/off half duty  
215 cycle, 30 min). After four days of survival, mice were transcardially perfused with 4% PFA  
216 and 0.5% glutaraldehyde in 0.1 M PB. After cryoprotection, the brains were horizontally  
217 sectioned at 60- $\mu$ m-thick and collected serially. Sections were then subjected to CO staining,  
218 standard ABC-amplification, peroxidase/benzidine reaction with nickel enhancement,  
219 mounted, dehydrated, cleared, and cover-slipped (Veinante and Deschênes, 1999). Individual  
220 lemniscal fibers were three-dimensionally reconstructed using a computer-assisted  
221 microscope system (Eclipse E800; Nikon) with a 40 $\times$  PlanApo objective lens (40 $\times$ /0.95;  
222 Nikon) and mapping program (NeuroLucida, RRID:SCR\_001775) (Honda et al., 2012).

223 Reconstructed data were quantitatively analyzed with Neurolucida Explore software and  
224 IGOR Pro software (RRID:SCR\_000325).

225

#### 226 *Retrograde labeling of ascending projection neurons in the brain stem*

227 One week after IONC, mice were anesthetized by 1–3% isoflurane, and placed on a  
228 stereotaxic apparatus. A small volume (0.15–0.30  $\mu$ l) of 0.5% cholera toxin B subunit (CTB)  
229 (C9903; Sigma) in 50 mM PBS was injected into the right V2 VPM (coordinates in mm:  
230 1.60–1.70 posterior and 1.80–1.90 lateral to the bregma, 3.00–3.20 below the dura) (Franklin  
231 and Paxinos, 2008) through a micro needle syringe (NF35BV and NANOFIL; WPI) by  
232 continuous pressure from a microsyringe pump (53311; Stoelting). After ejection, the needle  
233 tip was held in the V2 VPM for at least five minutes and then gently retracted to minimize  
234 leakage along the track. After 2–4 days of survival, mice were transcardially perfused and  
235 transverse brain stem sections (20  $\mu$ m thickness) were prepared using a freezing microtome.  
236 Alternating serial sections were subjected to CTB-immunostaining and the remaining were  
237 subjected to Nissl and/or CO staining. For fluorescent localization, the sections were  
238 incubated successively with 10% normal rabbit serum (NRS) in PBS-X for 30 min, 1:10,000  
239 goat anti-CTB antibody (List Biological Cat# 703, RRID:AB\_10013220) in PBS-X  
240 containing 0.12%  $\lambda$ -carrageenan, 1% NRS, and 0.02% sodium azide (PBS-XCR) overnight,  
241 3.75  $\mu$ g/ml biotinylated rabbit anti-goat IgG in PBS-XCR (BA-5000; Vector Laboratories) for  
242 2 h, and 2.5  $\mu$ g/ml Alexa Fluor 633-labeled streptavidin in PBS-X (S21375; Thermo Fisher  
243 Scientific) for 2 h. Sections were then mounted, counterstained, and cover-slipped.

244

#### 245 *Confocal microscopy*

246 Images of fluorescently stained sections were captured using a Zeiss LSM 710 scanning  
247 confocal microscope. Low-magnification images of 7- $\mu$ m-optical thickness were taken using

248 a 10×/0.45 objective lens (Plan-Apochromat; Carl Zeiss), 0.7× digital zoom, 1.58 μs pixel  
249 time, and four times frame average at 1,024 × 1,024 resolution. High-magnification images of  
250 1-μm-optical thickness were taken using a 63×/1.4 oil immersion lens (Plan-Apochromat;  
251 Carl Zeiss), 3.15 μs pixel time, and eight times frame average at 512 × 512 resolution. For  
252 quantitative measurements of VGluT2 or VGluT2-MAP2-double immunohistochemistry, two  
253 non-overlapping high-magnification regions of interest (ROIs) were acquired in the left and  
254 right V2 VPMs in four alternatively stained sections, respectively. The power of the lasers  
255 was 0.4–0.6 mW, which did not induce obvious fading.

256

#### 257 *Image analysis*

258 Raw image files were opened using a Carl Zeiss software (ZEN Digital Imaging for Light  
259 Microscopy, RRID:SCR\_013672), and each image was exported as an 8-bit tiff file. Area and  
260 intensity of tdTomato fluorescence in the left and right V2 VPM were measured using  
261 Analyze Particles command following auto-binarization by 8-bit, Enhance Contrast, and  
262 Threshold commands run as a single macro in ImageJ software (RRID:SCR\_003070) (Fig.  
263 1D). Density and size of VGluT2 puncta were also analyzed using a similar macro except  
264 Enhance Contract. The tdTomato-positive and -negative VGluT2 puncta in an image were  
265 automatically sorted using a macro in Photoshop software (Adobe Photoshop,  
266 RRID:SCR\_014199), and then subjected to ImageJ analyses. Dendritic and somatic VGluT2  
267 puncta on each MAP2-stained V2 VPM neuron and retrogradely-labeled brain stem neurons  
268 were manually counted using the Cell Counter plugin of ImageJ. For analysis of dendritic and  
269 somatic VGluT2 puncta on MAP2-stained V2 VPM neurons, five well-visualized neurons  
270 with large nucleus and thick proximal dendrites were randomly selected in each ROI. For  
271 analysis of CTB-labeled neurons, a 0.126 mm<sup>2</sup> ROI was placed at the center of corresponding  
272 brain stem region (e.g., PrV2) for each section and whole CTB-labeled neurons in the ROI

Takeuchi *et al.*, 2017

273 were then counted. Four alternatively stained sections for each brain stem region were  
274 analyzed for each animal. Images displayed with off-line magnification were processed by  
275 upscaling and noise-reduction algorithms (Tomasi and Manduchi, 1998; Freedman and Fattal,  
276 2011) using a house-made Windows software with GeForce technologies (GT 640; NVIDIA)  
277 (Takeuchi *et al.*, 2014).

278

279 *Identification of maxillary and mandibular regions in the Pr5 and SpI*

280 Maxillary and mandibular regions of the principle trigeminal nucleus, Pr5 (PrV2 and PrV3)  
281 were identified by region-specific Cre driver mouse lines, *Krox-20<sup>cre</sup>* and *Hoxa2-cre* (MGI  
282 ID: 3773535), respectively (Voiculescu *et al.*, 2000; Ren *et al.*, 2002). These drivers were  
283 crossed with tdTomato reporter line (Madisen *et al.*, 2010) or LacZ reporter line (MGI ID:  
284 5587997) (Kobayashi *et al.*, 2013). Recombination patterns were the same as previous reports  
285 using the same drives to identify PrV2 and PrV3: ventral and dorsal Pr5, corresponding to  
286 rhombomere 3 and 2, respectively (Oury *et al.*, 2006; Bechara *et al.*, 2015). Transgenically  
287 identified PrV2 and PrV3 regions were well consistent with the regions, where CTB-labeled  
288 primary afferent fibers from the whisker pad and lower jaw terminated, respectively.  
289 Maxillary and mandibular regions of the interpolar subnucleus of the spinal trigeminal nuclei  
290 (V2 SpI and V3 SpI) were also identified by the CTB-labeled primary afferent fiber terminals.

291

292 *Labeling of primary afferent fibers from peripheral tissue to the brain stem*

293 Mice were anesthetized by a ketamine/xylazine cocktail (80/10 mg/kg, i.p.) and placed under  
294 a dissecting microscope (Type 308795; Wild Heerbrugg). Five micro liter of 1% CTB with  
295 0.01% fast green FCF (Chroma-Gesellschaft) in 50 mM PBS was subcutaneously injected  
296 into the left whisker pad or the lower jaw through a micro needle syringe (NANOFIL; WPI).

297 After 2–4 days of survival, mice were transcardially perfused, cryo-blocked, sectioned, and  
298 stained as described above.

299

### 300 **Electrophysiology**

#### 301 *Patch-clamp recordings*

302 *Preparation of acute thalamic slices:* Mice were anesthetized with isoflurane (Abbott Japan)  
303 and decapitated. Parasagittal 300- $\mu\text{m}$ -thick thalamic slices (Arsenault and Zhang, 2006) were  
304 prepared using a vibrating blade microtome (VT1200S; Leica Microsystems) in an ice-cold  
305 cutting solution (in mM; 234 sucrose, 2.5 KCl, 1.25  $\text{NaH}_2\text{PO}_4$ , 10  $\text{MgCl}_2$ , 0.5  $\text{CaCl}_2$ , 25  
306  $\text{NaHCO}_3$ , 0.5 *myo*-inositol, and 11 glucose) equilibrated with 95% $\text{O}_2$ -5% $\text{CO}_2$ . Slices were  
307 recovered in artificial cerebrospinal fluid (ACSF) (in mM; 125 NaCl, 2.5 KCl, 1.25  $\text{NaH}_2\text{PO}_4$ ,  
308 1  $\text{MgSO}_4$ , 2  $\text{CaCl}_2$ , 26  $\text{NaHCO}_3$ , and 20 glucose) equilibrated with 95% $\text{O}_2$ -5% $\text{CO}_2$  at 32°C  
309 for 30 min and then kept at room temperature. A slice in a recording chamber was perfused by  
310 30°C–32°C ACSF at a rate of 2.5–3.0  $\text{ml min}^{-1}$ . During recordings, 10  $\mu\text{M}$  (-)-bicuculline  
311 methochloride, 1  $\mu\text{M}$  CGP55845, and 1  $\mu\text{M}$  strychnine were included in the superfusate.

312 *Whole-cell voltage-clamp recordings of lemniscal EPSCs:* The tip resistance of the  
313 patch pipette was 2–5  $\text{M}\Omega$  when filled with an intracellular solution: (in mM) 120  $\text{CsMeSO}_3$ ,  
314 10 HEPES, 1 EGTA, 2  $\text{MgCl}_2$ , 0.1  $\text{CaCl}_2$ , 20 NaCl, 5 QX-314, 2 ATP- $\text{Na}_2$ , 0.5 GTP- $\text{Na}$ , and  
315 0.5% biocytin (pH = 7.3, 290–300 mOsm). Liquid junction potential was not compensated.  
316 Recordings were made from V2 VPM neurons under the infrared-differential interference  
317 contrast view of an upright microscope as previously described (Anounymous et al. 2014).  
318 Recordings were performed using a MultiClamp700A amplifier (MDS) and an ITC-18  
319 AD/DA board (HEKA Elektronik) with IGOR Pro. Signals were filtered at 3 kHz and  
320 digitized at 50 kHz. The series resistance was compensated. If series resistance varied by >

321 20% or increased above 20 M $\Omega$ , the data were discarded. Data analysis was performed using  
322 IGOR Pro.

323 *Recordings of lemniscal fiber-mediated synaptic currents:* Lemniscal fiber-mediated  
324 synaptic currents were recorded as previously described (Takeuchi *et al.*, 2012). Briefly, a  
325 concentric bipolar electrode was placed on the medial lemniscal fiber bundle and electrical  
326 square pulses were then delivered at 0.1 Hz (100- $\mu$ s duration, typically 10–400  $\mu$ A). Paired-  
327 pulse depression of EPSCs were recorded. Evaluation of the number of lemniscal fibers  
328 innervating a recorded V2 VPM neuron was estimated by counting stepwise increments of  
329 EPSC amplitude in response to increasing stimulus intensity. Lemniscal fiber-mediated  
330 miniature EPSCs were recorded in modified ACSF, substituting Sr<sup>2+</sup> ions for Ca<sup>2+</sup> ions in the  
331 presence of 100  $\mu$ M DL-APV at -90 mV. Test stimulations were delivered at 0.1 Hz. The  
332 miniature EPSCs were detected and analyzed by a semi-automated IGOR Pro procedure  
333 (Takeuchi *et al.*, 2012).

334

335 *In vivo extracellular recordings of V2 VPM neurons*

336 One–two weeks or 1–3 months after IONC, mice were anesthetized with 1–3% isoflurane,  
337 and placed on a stereotaxic apparatus. Rectal temperature was maintained at 36°C–37°C using  
338 a DC temperature controller (40-90-8D; FHC). Stages of anesthesia were maintained by  
339 confirming the lack of vibrissae movements and eyelid reflex (Friedberg *et al.*, 1999; Miyata  
340 *et al.*, 2003). The head position was adjusted until the heights of the bregma and the lambda  
341 became equal. A small craniotomy was operated at the skull above the right V2 VPM, and a  
342 16-channel silicon probe (A1x16-5mm-25-177 or A1x16-Poly2-5mm-50s; NeuroNexus) or a  
343 single microelectrode (2–4 M $\Omega$ ; FHC or Unique Medical) was vertically inserted into the V2  
344 VPM using a stepper motor manipulator (coordinates in mm: 1.60–1.90 posterior and 1.70–  
345 2.10 lateral to the bregma, 3.00–3.50 below the dura) (Franklin and Paxinos, 2008). A screw-

346 type reference electrode (TN204-089B) was fixed in the rostral skull. Receptive fields of V2  
347 VPM neurons were identified as multi-unit neural firings in response to tactile stimuli  
348 throughout the body. This receptive field mapping was conducted at 50  $\mu\text{m}$  interval along  
349 electrode track. At each recording site, the receptive fields were roughly surveyed at first  
350 using paint brushes, metal probes (FST), and air-puff through a 26G needle controlled by a  
351 pneumatic pico pump (PV830; WPI). The size and precise location of each receptive field was  
352 then identified using von Frey filaments (Semmes-Weinstein monofilaments; Stoelting),  
353 and/or a piezoelectric device (M-2629B; MESS-TEK) (Simons, 1983) if it included large  
354 whiskers. The timing of these stimuli was monitored using a CMOS camera (MQ003CG-CM;  
355 Ximea). Neural activity was processed with an OmniplexD 16 ch system (Plexon) or an  
356 extracellular amplifier (2400A; Dagan), filtered at 0.25–10 kHz, and digitized at 40–50 kHz  
357 with OmniPlex software (RRID:SCR\_014803) or Spike2 software (RRID:SCR\_000903).  
358 After recordings, several recording sites were marked by feeding anodal currents through the  
359 electrode (typically 5  $\mu\text{A}$ , 10 s). The mice were then deeply anesthetized with pentobarbital  
360 (120 mg/kg, i.p.) and transcardially perfused with ice-cold saline followed by 4% PFA and  
361 0.2% picric acid in 0.1 M PB. The brains were postfixed overnight, then coronally sectioned  
362 at 50  $\mu\text{m}$  thickness using a vibrating blade microtome (VT1000S; Leica Microsystems). The  
363 sections were then mounted, counterstained with fluoro-Nissl staining, and cover-slipped.  
364 Images were taken using a confocal laser scanning microscope as described above. Recording  
365 sites were reconstructed using NeuroLucida software. Only recordings made in the V2 VPM,  
366 which was easily recognized by strong tdTomato fluorescence from PrV2-origin lemniscal  
367 fibers, were analyzed. Spikes were detected and sorted by custom software written in  
368 MATLAB (RRID:SCR\_001622) or IGOR Pro (Quiroga *et al.*, 2004).

369

370 **Tactile sensory test**

371 Mice were habituated to being held in the experimenter's hands and then to von Frey filament  
372 application to their maxillary and mandibular regions one or two week(s) prior to IONC  
373 (Seino *et al.*, 2009). On P21 or P60, the ION was cut or sham-operated as described above. To  
374 evaluate escape thresholds, quantitative mechanical stimuli via von Frey filaments with  
375 approximately equal logarithmic bending forces (0.02, 0.03, 0.07, 0.16, 0.4, 0.6, 1.0, 1.4, and  
376 2.0 g forces, respectively) were applied to the maxillary and mandibular regions in ascending  
377 order. Each von Frey filament was applied five times. If mice showed positive withdrawal  
378 responses—e.g. brisk withdrawal of the head, face-grooming strokes directed to the  
379 stimulated facial area—at least three times, the bending force of that filament was defined as  
380 the escape threshold. If mice did not show any responses to 2.0 g of force, the escape  
381 threshold was set at 2.0 g (cutoff). This series of assessment was repeated three times and the  
382 average of the three withdrawal thresholds was recorded for that day.

383

#### 384 **Statistical analysis**

385 Unless otherwise noted, all values are given as means  $\pm$  s.d. between observations. Means  $\pm$   
386 s.d. between animals were also given in the text as parenthesized. Appropriate statistical tests  
387 were performed depending on experimental designs; for example when eight non-overlapping  
388 image acquisitions were made on brain sections from each sham or IONC mouse, two-way  
389 repeated measures ANOVA was employed to extract major effect of operation or survival  
390 time on measured values (the other effect was animal) (Glantz, 2011). Details of statistical  
391 analyses were given in respective results, figure legends, and Table 3 (Statistical Table). *Post-*  
392 *hoc* power analysis was performed using G\*Power3 software (<http://www.gpower.hhu.de/>)  
393 (RRID:SCR\_013726) (Faul *et al.*, 2007). R software was applied for statistical tests (R Project  
394 for Statistical Computing, RRID:SCR\_001905). The significance level was set at  $P < 0.05$ .

395

396 **Results**397 **Injury of primary whisker sensory nerve decreased PrV2-origin lemniscal fibers in V2**398 **VPM.**

399 To selectively assess anatomical remodeling of the PrV2-origin lemniscal fibers, we  
400 employed a Krox20-Ai14 mouse line (Fig. 1A), in which most of the projection neurons in the  
401 PrV2 specifically express tdTomato (Takeuchi *et al.*, 2014). In Krox20-Ai14 mice, tdTomato  
402 was specifically found in the V2 region of the Pr5 (PrV2), but not in the V3 region (PrV3)  
403 (Fig. 1C<sub>2</sub>) or other trigeminal nuclei (data not shown). IONC (Fig. 1B) did not alter this  
404 specific expression pattern (Fig. 1C<sub>2</sub>). Projection neurons in the PrV2 were thoroughly  
405 visualized from the soma to synaptic terminals in the V2 VPM (Fig. 1C, D). Unilateral IONC  
406 significantly decreased macroscopically observed tdTomato signal intensity and the  
407 occupying area in the contralateral V2 VPM [contra/ipsi ratio:  $0.86 \pm 0.04$  and  $0.74 \pm 0.18$   
408 ( $0.86 \pm 0.06$  and  $0.77 \pm 0.26$  between animals) for intensity and area, respectively,  $***p <$   
409  $0.001^a$ , main effect of IONC,  $F_{1,18} > 52.3$  for both; Fig. 1D, E]. These results suggest that  
410 IONC significantly reduces the PrV2-origin lemniscal fiber territory in the V2 VPM.

411

412 **IONC increased non-PrV2-origin lemniscal fiber terminals in V2 VPM related to**  
413 **multiple lemniscal fiber innervations onto a V2 VPM neuron.**

414 We have previously demonstrated that complete transection of ION newly recruits additional  
415 multiple lemniscal fibers onto a V2 VPM neuron (multiple innervation) (Takeuchi *et al.*,  
416 2012). To reveal somatotopic reorganization underlying this rewiring, we conducted VGluT2-  
417 immunohistochemistry in the V2 VPM of Krox20-Ai14 mice after IONC; VGluT2 is a  
418 marker of lemniscal fiber terminals (Graziano *et al.*, 2008). Previously, we have shown that in  
419 the V2 VPM of Krox20-Ai14 mice, PrV2-origin and non-PrV2-origin lemniscal fiber  
420 terminals are represented as tdTomato (tdT)-positive and -negative VGluT2 puncta,

421 respectively (Takeuchi *et al.*, 2014). Here we found that, after IONC, the density of tdT-  
422 positive VGluT2 puncta in the contralateral V2 VPM significantly decreased [ $111.4 \pm 9.7$  and  
423  $87.3 \pm 14.1$  ( $111.4 \pm 27.5$  and  $87.3 \pm 39.8$  between animals) in  $18,212 \mu\text{m}^2$  ROI for sham and  
424 IONC, respectively;  $***p < 0.001^b$ , main effect of IONC,  $F_{1,222} = 33.1$ ], whereas the density  
425 of tdT-negative ones increased [ $25.7 \pm 11.8$  and  $57.1 \pm 28.1$  ( $25.6 \pm 14.8$  and  $57.1 \pm 44.0$ ) in  
426  $18,212 \mu\text{m}^2$  ROI;  $***p < 0.001^c$ ,  $F_{1,222} = 73.0$ ] (Fig. 2A, B). The total density of VGluT2  
427 puncta in the contralateral V2 VPM (tdT-positive + tdT-negative) did not differ between sham  
428 and IONC groups [ $137.1 \pm 26.2$  and  $144.3 \pm 40.7$  ( $137.1 \pm 38.1$  and  $144.3 \pm 76.4$ ) in  $18,212$   
429  $\mu\text{m}^2$  ROI;  $p = 0.221^d$ ,  $F_{1,222} = 1.5$ ]. Thus, the percentage of tdT-positive VGluT2 puncta in the  
430 contralateral V2 VPM significantly decreased after IONC [ $81.3 \pm 7.4\%$  and  $60.8 \pm 13.5\%$   
431 ( $81.3 \pm 6.7$  and  $60.8 \pm 14.7$ );  $***p < 0.001^e$ ,  $F_{1,222} = 102.2$ ; Fig. 2C]. These results indicate  
432 considerable retraction of PrV2-origin lemniscal fibers and invasion of non-PrV2-origin ones  
433 in the V2 VPM after IONC.

434         Given the results above, we then examined whether IONC increases the number of  
435 contacts between non-PrV2-origin VGluT2 puncta and a V2 VPM neuron. VGluT2 puncta  
436 could be observed both on the soma and proximal dendrites of V2 VPM neurons as previously  
437 reported (Matthews and Faciane, 1977; Liu *et al.*, 1995; Takeuchi *et al.*, 2014) (Fig. 2A,  
438 bottom). In the contralateral V2 VPM of the IONC group, tdT-negative puncta formed  
439 contacts on V2 VPM neurons, and their numbers on each V2 VPM neuron in  $1\text{-}\mu\text{m}$ -thick  
440 optical section significantly increased on both the soma and dendrites [soma:  $0.73 \pm 1.26$  and  
441  $1.54 \pm 1.63$  ( $0.69 \pm 1.30$  and  $1.54 \pm 2.75$  between animals) for sham and IONC, respectively;  
442 dendrites:  $0.49 \pm 0.86$  and  $0.81 \pm 1.01$  ( $0.49 \pm 0.71$  and  $0.82 \pm 2.04$ );  $*p < 0.018^f$ , main effect  
443 of IONC,  $F_{1,180} > 5.7$  for both; Fig. 2A bottom and 2D]. In contrast, both somatic and  
444 dendritic tdT-positive VGluT2 puncta significantly decreased [soma:  $1.80 \pm 1.42$  and  $1.34 \pm$   
445  $1.60$  ( $1.78 \pm 1.10$  and  $1.35 \pm 2.74$ ); dendrites:  $1.32 \pm 1.19$  and  $0.71 \pm 0.92$  ( $1.37 \pm 1.48$  and

446  $0.71 \pm 1.60$ );  $*p < 0.037^g$ ,  $F_{1,180} > 4.4$ ; Fig. 2A bottom and 2D]. These results suggest that  
447 after IONC, newly recruited non-PrV2-origin fibers form new synaptic contacts both on the  
448 soma and dendrites of V2 VPM neurons while PrV2-origin fibers retract from preexisting  
449 contacts. When we classified each V2 VPM neuron by the origin of converging afferent fibers  
450 on the neuron, in the control conditions, 76–77% of V2 VPM neurons received only tdT-  
451 positive VGluT2 puncta on the soma or proximal dendrites, 22–23% of V2 VPM neurons  
452 received only tdT-negative VGluT2 puncta, but only 1% of V2 VPM neurons received both  
453 tdT-positive and -negative ones. IONC decreased the proportion of V2 VPM neurons  
454 receiving only tdT-positive VGluT2 puncta to 46% and increased the proportion of those that  
455 received only tdT-negative ones to 52% [ $p = 0.004^h$ ,  $\chi^2 = 10.81$  ( $n = 188$  neurons)]. Even after  
456 IONC, V2 VPM neurons receiving both tdT-positive and -negative ones were still rare (2%).

457       Next, we examined the correlation between the emergence of tdT-negative VGluT2  
458 puncta and electrophysiologically assessed multiple innervation of lemniscal fibers onto a V2  
459 VPM neuron after IONC (Takeuchi *et al.*, 2012). On postoperative day (POD) 5–6, the  
460 number of lemniscal fiber-mediated EPSC steps in a V2 VPM neuron increased and became  
461 statistically significant (Fig. 2E bottom) (Takeuchi *et al.*, 2012). tdT-negative VGluT2 puncta  
462 also increased with a time course matching the EPSC steps (Fig. 2E). Importantly, the  
463 percentage of tdT-negative VGluT2 puncta and EPSC steps were significantly correlated ( $r =$   
464  $0.87$ ,  $**p = 0.002^i$ ,  $t_7 = 4.63$ ; Fig. 2F). Here we also explored mechanisms underlying  
465 lemniscal fiber remodeling in the V2 VPM. Whisker deprivation from P21 did not decrease  
466 tdT-positive VGluT2 puncta [ $92.2 \pm 29.9$  and  $97.0 \pm 27.7$  ( $105.8 \pm 69.8$  and  $97.0 \pm 12.9$   
467 between animals) in  $18,212 \mu\text{m}^2$  ROI for intact and whisker deprivation, respectively],  
468 increase tdT-negative ones [ $18.6 \pm 8.0$  and  $19.5 \pm 7.1$  ( $18.2 \pm 11.4$  and  $19.5 \pm 7.4$ ) in  $18,212$   
469  $\mu\text{m}^2$  ROI], or change the percentage of tdT-positive ones [ $81.3 \pm 12.9\%$  and  $82.7 \pm 6.7\%$   
470 ( $83.4 \pm 21.0\%$  and  $82.7 \pm 8.2\%$ )] in the contralateral V2 VPM ( $p > 0.549^j$ , main effect of

471 whisker deprivation,  $F_{1,36} < 0.4$  for all; Fig. 2G–I). Importantly, whisker deprivation does not  
472 recruit multiple lemniscal fiber innervations (Takeuchi *et al.*, 2012), suggesting an injury-  
473 induced, but not sensory experience-dependent, mechanism. Hence these results suggest that  
474 multiple lemniscal fiber innervations onto a V2 VPM neuron after IONC are mediated at least  
475 partially by newly recruited lemniscal fibers of non-PrV2-origin and the extent of the multiple  
476 innervation is predictable by anatomical assessments using Krox20-Ai14 mice.

477

478 **IONC decreased size of PrV2-origin lemniscal fiber terminals in V2 VPM and amplitude**  
479 **of lemniscal fiber-derived miniature EPSCs.**

480 To estimate the strength of lemniscal fiber synapses specifically after IONC, we measured the  
481 sizes of tdT-positive and -negative VGluT2 puncta in the contralateral V2 VPM (Fig. 3).  
482 IONC operation selectively decreased the size of tdT-positive VGluT2 puncta [ $2.28 \pm 0.20$   
483 and  $2.05 \pm 0.24 \mu\text{m}^2$  ( $2.28 \pm 0.123$  and  $2.02 \pm 0.29 \mu\text{m}^2$  between animals) for sham and  
484 IONC;  $p < 0.001^k$ , main effect of IONC,  $F_{1,222} = 21.2$ ] and the distributions of sham and  
485 IONC groups were significantly different ( $***p < 0.001^l$ ,  $D = 0.08$ ; Fig. 3A, B). However,  
486 sizes of tdT-negative ones were not different between sham and IONC groups [ $2.05 \pm 0.31$  vs.  
487  $2.05 \pm 0.24 \mu\text{m}^2$  ( $2.05 \pm 0.37$  and  $2.05 \pm 0.18 \mu\text{m}^2$ );  $p = 0.697^m$ ,  $F_{1,222} = 0.152$ ]. Consistent  
488 with these anatomical results, the amplitude of miniature EPSCs evoked by electrical  
489 stimulation of the lemniscal fiber bundle significantly decreased after IONC ( $***p < 0.001^n$ ,  
490  $D = 0.28$ ; Fig. 3C, D) (Takeuchi *et al.*, 2012). These results suggest fiber-origin-specific  
491 weakening of lemniscal fiber synapses after IONC.

492

493 **IONC induced morphological changes of PrV2-origin lemniscal fibers in V2 VPM.**

494 To establish a precise anatomical basis for lemniscal fiber remodeling after IONC, we  
495 visualized individual PrV2-origin lemniscal fibers at single axon resolution using an

496 anterograde tracer BDA (Fig. 4A, B). Each single PrV2-origin lemniscal fiber was serially  
497 traced, reconstructed, and quantitatively analyzed (Fig. 4C–E). In the sham group, each PrV2-  
498 origin lemniscal fiber proceeded from caudal to rostral in the V2 VPM with few branches, and  
499 then exhibited bushy terminal arborization with clustered numerous axon terminals and  
500 synaptic boutons within 100  $\mu\text{m}$  in diameter (Fig. 4B, C<sub>1</sub>–E<sub>1</sub>). After IONC, the numbers of  
501 boutons [ $23.4 \pm 15.0$  between fibers ( $18.6 \pm 17.3$  between animals)], terminals [ $16.4 \pm 8.9$   
502 ( $14.5 \pm 4.4$ )], and branches [ $13.8 \pm 8.1$  ( $12.7 \pm 3.1$ )] within each fiber were all significantly  
503 decreased compared with those of the sham group [ $40.5 \pm 25.0$  ( $50.9 \pm 17.4$ ),  $25.4 \pm 15.7$   
504 ( $32.7 \pm 12.3$ ), and  $22.3 \pm 14.1$  ( $28.1 \pm 9.7$ ), respectively;  $**p < 0.005^o$ , main effect of IONC,  
505  $F_{1,59} > 8.5$  for all; Fig. 4C<sub>2</sub>]. IONC also made axon branches much farther away from the  
506 barycenter of terminal arborization ( $***p < 0.001^p$ ,  $D = 0.17$ ; Fig. 4D<sub>2</sub> right). If branches  
507 more than 50  $\mu\text{m}$  away from the barycenter are defined as ectopic branches, then the  
508 percentage of ectopic branches within each PrV2-origin lemniscal fiber tended to increase  
509 after IONC [ $18.8 \pm 20.4\%$  ( $25.9 \pm 22.7\%$ )] compared with that in the sham group [ $9.6 \pm$   
510  $12.0\%$  ( $9.5 \pm 6.2\%$ );  $p = 0.065^q$ ,  $F_{1,59} = 3.5$ ; Fig. 4D<sub>2</sub> left]. Furthermore, IONC increased the  
511 distances between bouton pairs and terminal pairs within each PrV2-origin lemniscal fiber,  
512 indicating diverging innervation patterns ( $***p < 0.001^r$ ,  $D > 0.13$  for both; Fig. 4E). These  
513 results indicate that each PrV2-origin lemniscal fiber is weakened but has diverging  
514 innervation patterns in the V2 VPM after IONC.

515

516 **IONC induced additional lemniscal fiber innervations from non-V2 brain stem nuclei to**  
517 **V2 VPM.**

518 What are the origins of the non-PrV2-origin lemniscal fiber terminals in the V2 VPM after  
519 IONC? To address this question, CTB—a retrograde neural tracer—was locally injected in the  
520 V2 VPM as described previously (Takeuchi *et al.*, 2014) (Fig. 5A). In the sham group,

521 retrogradely labeled projection neurons in the brain stem were observed almost exclusively in  
522 the contralateral PrV2 and V2 SpI [ $122.2 \pm 69.5$  and  $20.7 \pm 11.9$  ( $122.1 \pm 161.2$  and  $20.7 \pm$   
523  $26.8$  between animals), respectively; three mice (four  $0.126 \text{ mm}^2$  ROIs from separate sections  
524 from each mouse); Fig. 5B–D]. Surprisingly, after IONC, additionally significantly labeled  
525 neurons were observed in the PrV3, V3 SpI, and dorsal column nuclei (DCN) [ $45.4 \pm 51.4$ ,  
526  $18.8 \pm 10.8$ , and  $53.6 \pm 24.0$  ( $45.4 \pm 109.0$ ,  $18.8 \pm 20.6$ , and  $53.6 \pm 52.3$ ), respectively;  $***p <$   
527  $0.001^s$ , main effect of IONC,  $F_{1,21} > 74.4$  for all, four mice], whereas retrograde labelings in  
528 those nuclei were negligible in the sham group [ $0.3 \pm 0.7$ ,  $2.4 \pm 1.4$ , and  $4.2 \pm 3.9$  ( $0.3 \pm 1.2$ ,  
529  $2.4 \pm 2.6$ , and  $4.2 \pm 5.1$ ), respectively; Fig. 5B–D]. The retrogradely labeled neurons in such  
530 ectopic regions were all tdT-negative. Ipsilateral labelings were not observed in the sham or  
531 IONC group. After IONC, labeled neurons increased also in the caudal subnucleus of the  
532 spinal trigeminal nuclei (SpC) although the number was still relatively small [ $1.2 \pm 1.4$  and  
533  $5.5 \pm 2.4$  ( $1.2 \pm 3.2$  and  $5.5 \pm 3.2$ ) for sham and IONC, respectively;  $p < 0.001^t$ , main effect of  
534 IONC,  $F_{1,21} = 49.2$ , data not shown]. These results indicate that the origins of non-PrV2-  
535 origin lemniscal fiber terminals in the V2 VPM after IONC include V3 subregions of the  
536 trigeminal nuclei and DCN. Although ectopic innervations from even non-trigeminal brain  
537 stem nuclei such as the DCN to the V2 VPM after IONC were suggested, normal cyto-  
538 architecture and delineation were maintained over the trigeminal nuclei and the DCN (Fig.  
539 5B<sub>1</sub>, C). There was no collapse of boundaries between trigeminal nuclei and DCN after IONC  
540 even at the closest site between them (Fig. 5E)

541

#### 542 **Alterations in receptive fields and behavior after IONC**

543 Given the results of retrograde tracing, possible receptive field changes of V2 VPM neurons  
544 after IONC were examined. In anesthetized mice, multiunit activity of V2 VPM neurons was  
545 recorded in response to mechanical stimuli throughout the face and body (six and five mice

546 for sham and IONC, respectively; Fig. 6A–D). In the sham group, receptive fields were  
547 always confined to the V2 region of the contralateral face: 39 V2-responsive sites and 3 non-  
548 responsive sites of 42 total mapped sites in the V2 VPM (Table 1). These responses were  
549 always reliable and have small receptive fields confined to typically one or two whiskers (Fig.  
550 6C (i), (ii)). However, in the IONC group, receptive fields of V2 VPM neurons were rarely  
551 observed on the V2 region of the face (in total, three out of 65 mapped sites); these infrequent  
552 V2 responses might have been mediated by the regenerated ION (Waite, 1984; Kis *et al.*,  
553 1999) or direct tension to proximal stump of the ION and/or adjacent region when a heavy  
554 von Frey filament was applied to the whisker pad. Importantly, after IONC, receptive fields  
555 were observed on the V3 region of the face such as lower jaw and/or also on the body such as  
556 neck, chest, and back (in total, nine V3-responsive sites, 11 DCN-region-responsive sites, and  
557 50 non-responsive sites out of 65 mapped sites) (Fig. 6C (iii), D and Table 1). The non-  
558 trigeminal receptive fields (DCN-region-responsive sites) in the V2 VPM were not confined  
559 to the ventral most recording sites, which is adjacent to the VPL, but were distributed along  
560 the electrode tracks (Fig. 6C, red and magenta circles). The ectopic receptive fields were  
561 spatially consistent with ectopically labeled projection neurons in the V3 regions of trigeminal  
562 nuclei and DCN (Fig. 5). These ectopic responses were not as reliable as normal responses in  
563 the sham group, which means repeated stimulations on the ectopic receptive fields do not  
564 always fire V2 VPM neurons as those on normal receptive field in the sham group (50–75%  
565 and 100% in success rate approximately for the IONC and sham groups, respectively, when  
566 similar light tactile stimuli were applied at 0.1 Hz). This observation was very consistent with  
567 the fact that there exists a subset of much weaker lemniscal fiber-mediated EPSCs after IONC  
568 in the VPM, which may not be strong enough to drive reliable firing of postsynaptic V2 VPM  
569 neurons (Takeuchi *et al.*, 2012). The possible functional immaturity of newly-invading  
570 ectopic fibers could explain a discrepancy between small number of V3- and DCN-region-

571 responsive sites in receptive field recordings and extensive ectopic retrograde labelings in V3  
572 and DCN regions (Figs. 5 and 6). In addition, the size of the ectopic receptive fields was  
573 much larger (Fig. 6D). These results suggest that IONC-induced remodeling of lemniscal  
574 fibers, including both PrV2-origin and non-PrV2-origin ones, establishes ectopic sensory  
575 pathways from non-V2 peripheral tissue, including the V3 region of the face and the body, to  
576 the V2 VPM within one week.

577 To investigate the impact of the IONC-induced lemniscal fiber remodeling on  
578 somatotopic sensation, we investigated nociceptive pain behavior by measuring the escape  
579 threshold in response to mechanical stimuli applied to the face using the von Frey test (Fig.  
580 6E). In the IONC group, the escape threshold in response to mechanical stimuli to the V2  
581 region significantly increased (mostly up to cutoff: 2 g). Note that although normalized escape  
582 thresholds of the IONC group tended to decline over the postoperative days, they are at least  
583 10 times larger than those of the sham group over two weeks after IONC (Fig. 6E). The  
584 decline of normalized escape thresholds was mediated mainly by increase in the sham group  
585 due to growth and partial by decrease in the IONC group possibly due to regeneration of the  
586 transected ION. Absolute escape thresholds of the V2 region on POD1 and POD11 were  $0.04$   
587  $\pm 0.02$  and  $0.14 \pm 0.18$  for the sham group, and  $2.00 \pm 0.00$  and  $1.54 \pm 0.37$  for the IONC  
588 group, respectively. This partial recovery in escape thresholds of V2 region might have been  
589 due to the same causes for infrequent V2 region receptive fields of V2 VPM neurons  
590 described above: ION regeneration and propagations of applied tension to surrounding  
591 regions. One to two weeks after IONC, escape thresholds in response to mechanical stimuli to  
592 the V3 region (lower jaw) significantly decreased compared with those in the sham group ( $p <$   
593  $0.001^{\text{a}}$ , two-way repeated measures ANOVA,  $F_{1,212} = 34.8$ ;  $*p < 0.05$ ,  $**p < 0.01$ , *post-hoc*  
594 Tukey HSD test; Fig. 6E). Decrease in the escape threshold became statistically significant  
595 from POD6, which was temporally consistent with that of the lemniscal fiber remodeling (Fig.

596 2) (Takeuchi *et al.*, 2012). These results indicate allodynia-like extraterritorial mechanical  
597 hypersensitivity in the mandibular region that spatially corresponds to ectopic receptive fields  
598 of V2 VPM neurons after IONC, and these changes were temporally consistent with lemniscal  
599 fiber remodeling.

600

601 **Long-lasting lemniscal fiber remodeling, reorganization of receptive field, and**  
602 **behavioral changes after IONC**

603 Next, we investigated the duration of the IONC-induced changes (Fig. 7A). One month (1 m)  
604 and even three months (3 m) after IONC, tdTomato fluorescence intensity and the occupying  
605 area in the contralateral V2 VPM remained significantly reduced [contra/ipsi ratio of signal  
606 intensity:  $0.82 \pm 0.11$  and  $0.93 \pm 0.09$  ( $0.82 \pm 0.13$  and  $0.93 \pm 0.09$  between animals) for 1 m  
607 and 3 m, respectively; contra/ipsi ratio of signal area:  $0.73 \pm 0.21$  and  $0.69 \pm 0.17$  ( $0.73 \pm 0.25$   
608 and  $0.69 \pm 0.27$ ) for 1 m and 3 m;  $**p < 0.01^v$ ,  $***p < 0.001^v$ , main effect of IONC,  $F_{1,24} >$   
609 8.0 for all; Fig. 7B, D]. Although there was some recovery between one and three months  
610 after IONC in tdTomato fluorescence intensity ( $**p < 0.01^w$ , main effect of survival time,  
611  $F_{1,24} = 10.9$ ), there was no recovery in occupying area between one and three months after  
612 IONC ( $p = 0.439^x$ ,  $F_{1,24} = 0.6$ ; Fig. 7B, D). Even three months after IONC, the density of tdT-  
613 positive VGluT2 puncta remained lower [ $105.0 \pm 27.6$  and  $68.7 \pm 38.7$  ( $105.0 \pm 45.2$  and  $68.7$   
614  $\pm 62.2$  between animals) in  $18,212 \mu\text{m}^2$  ROI for sham and IONC, respectively;  $***p < 0.001^y$ ,  
615 main effect of IONC,  $F_{1,56} = 22.7$ ] and that of tdT-negative ones remained higher [ $28.0 \pm 17.8$   
616 and  $52.5 \pm 26.3$  ( $28.0 \pm 39.2$  and  $52.5 \pm 15.3$ ) in  $18,212 \mu\text{m}^2$  ROI;  $***p < 0.001^z$ ,  $F_{1,56} = 20.6$ ;  
617 Fig. 7C, E]. Consequently, the proportion of tdT-positive puncta remained lower [ $79.2 \pm$   
618  $11.5\%$  and  $53.9 \pm 21.8\%$  ( $79.2 \pm 20.4\%$  and  $53.9 \pm 23.4$ ,  $***p < 0.001^{aa}$ ,  $F_{1,56} = 35.9$ ; Fig. 7C,  
619 F]. Consistent with this long-lasting and large-scale lemniscal fiber remodeling, ectopic  
620 receptive fields were found more than one month after IONC (n = three mice for each group).

621 Like the results in Figure 6, receptive fields of V2 VPM neurons typically included the V3  
622 region of the face (sham: 20 V2-responsive sites, one non-responsive site out of 21 total  
623 mapped sites; IONC: seven V2-responsive sites, eight V3-responsive sites, 38 non-responsive  
624 sites out of 52 total mapped sites) (Fig. 7G, H and Table 2). The size of such ectopic receptive  
625 fields was much larger than that in the sham group. Furthermore, more than three months after  
626 IONC, a lowered escape threshold in response to mechanical stimuli on the V3 region still  
627 existed ( $p < 0.001^{bb}$ , two-way repeated measures ANOVA,  $F_{1,50} = 51.2$ ;  $*p < 0.05$ ,  $**p < 0.01$ ,  
628 *post-hoc* Tukey HSD test; Fig. 7I). These results indicate that the IONC-induced lemniscal  
629 fiber remodeling in the V2 VPM, ectopic receptive fields of V2 VPM neurons, and ectopic  
630 mechanical hypersensitivity are all long-lasting with temporal consistency among them.

631

#### 632 **IONC induced lemniscal fiber remodeling in the adult**

633 We also investigated whether IONC in adult animals induced the lemniscal fiber remodeling  
634 in the V2 VPM (Fig. 8A). One week after IONC in adults (P60), we macroscopically observed  
635 significantly decreased tdTomato fluorescence intensity and occupying area in the  
636 contralateral V2 VPM [contra/ipsi ratio:  $0.89 \pm 0.05$  and  $0.80 \pm 0.09$  ( $0.89 \pm 0.05$  and  $0.80 \pm$   
637  $0.04$  between animals) for intensity and area,  $***p < 0.001^{cc}$ , main effect of IONC,  $F_{1,26} >$   
638  $14.5$  for both; Fig. 8B, C]. After the adult IONC procedure, the density of tdT-positive  
639 VGluT2 puncta significantly decreased [ $83.8 \pm 29.0$  and  $64.5 \pm 28.1$  ( $83.8 \pm 33.1$  and  $64.5 \pm$   
640  $21.3$  between animals) in  $18,212 \mu\text{m}^2$  ROI for sham and IONC, respectively;  $*p = 0.024^{dd}$ ,  
641 main effect of IONC,  $F_{1,42} = 5.5$ ], whereas that of tdT-negative ones increased [ $14.8 \pm 7.5$  and  
642  $31.3 \pm 14.4$  ( $14.8 \pm 12.7$  and  $31.3 \pm 4.0$ ) in  $18,212 \mu\text{m}^2$  ROI;  $***p < 0.001^{ee}$ ,  $F_{1,42} = 24.1$ ] in  
643 the contralateral V2 VPM (Fig. 8D, E). The total density of VGluT2 puncta did not differ  
644 between sham and IONC groups [ $98.6 \pm 28.8$  and  $95.8 \pm 20.0$  ( $98.6 \pm 40.3$  and  $95.8 \pm 17.8$ ) in  
645  $18,212 \mu\text{m}^2$  ROI;  $p = 0.686^{ff}$ ,  $F_{1,42} = 0.166$ ]. Accordingly, the percentage of tdT-positive

Takeuchi *et al.*, 2017

646 VGlut2 puncta in the contralateral V2 VPM significantly decreased after IONC even in  
647 adults [ $83.9 \pm 8.8\%$  and  $65.2 \pm 18.2\%$  ( $83.9 \pm 12.6\%$  and  $65.2 \pm 6.9\%$ );  $***p < 0.001^{eg}$ ,  $F_{1,42}$   
648 = 19.6; Fig. 8D, F]. Thus, it is likely that the IONC-induced lemniscal fiber remodeling has  
649 no critical time window.  
650

651 **Discussion**

652 *Neural circuitry mechanisms underlying large-scale somatotopic reorganization in the*  
653 *thalamus after peripheral sensory nerve injury*

654 Using a Krox20-Ai14 transgenic mouse line combined with VGluT2 immunohistochemistry,  
655 we successfully distinguished somatotopic information for remodeled lemniscal fiber at  
656 single-bouton resolution after IONC. We found that the number of EPSC steps and percentage  
657 of non-PrV2-origin lemniscal fiber terminals in the V2 VPM were significantly correlated  
658 (Fig. 2). The correlation suggests that multiple non-PrV2-origin lemniscal fibers converged  
659 onto a V2 VPM neuron after IONC. Whisker deprivation, on the other hand, induced neither  
660 multiple lemniscal fiber innervations onto a V2 VPM neuron (Takeuchi *et al.*, 2012) nor  
661 invasion of ectopic inputs (Fig. 2), confirming that these changes were induced by nerve  
662 injury itself, but not by sensory deprivation. Furthermore, the results shown in Figure 5  
663 demonstrated clearly that the lemniscal fiber remodeling is associated with new projections of  
664 ectopic afferent inputs from large-scale uninjured origins, including PrV3, V3 SpI, and DCN  
665 to the V2 VPM. It is likely that sprouting collaterals of V3 VPM-targeted and/or VPL-  
666 targeted lemniscal fibers originating from these uninjured brain stem nuclei constitutes a  
667 neural circuitry mechanism underlying the somatotopic reorganization after IONC. This  
668 speculation is quite reasonable because the V3 VPM and VPL are located in regions adjacent  
669 to the V2 VPM (Franklin and Paxinos, 2008). Taken together, the present study provides clear  
670 evidence of a neural circuitry mechanism underlying large-scale somatotopic reorganization  
671 in the thalamus after peripheral sensory nerve injury.

672

673 *Spatial and temporal consistency among lemniscal fiber remodeling, reorganization of*  
674 *receptive fields, and abnormal ectopic sensation after IONC*

675 The somatotopic reorganization underlying anatomical remodeling of lemniscal fibers could  
676 be further expanded to changes in receptive fields of V2 VPM neurons and behavioral level in  
677 terms of spatial and temporal consistency. Spatially, ectopic non-PrV2-origin lemniscal fibers,  
678 ectopic receptive fields, and extraterritorial mechanical hypersensitivity all occurred on the  
679 mandibular and DCN regions (Figs. 5 and 6). Temporally, we confirmed that all changes in  
680 our experiments at different hierarchical levels, including multiple lemniscal fiber innervation  
681 onto a V2 VPM neuron (Takeuchi *et al.*, 2012), remodeling of lemniscal fiber synapses in the  
682 V2 VPM (Fig. 5), changes of PrV2-origin lemniscal fiber terminal morphology (Fig. 4),  
683 appearance of ectopic receptive fields of V2 VPM neurons (Fig. 6) and extraterritorial  
684 mechanical hypersensitivity on the mandibular region (Fig. 6), concomitantly developed  
685 within one week after IONC. These changes followed a similar time course over three months  
686 (Fig. 7), which is clearly different from the time course of unmasking of preexisting but latent  
687 neural pathways (unmasking emerges within a few minutes and lasts several hours after  
688 lidocaine-mediated deafferentation) (Nicoletis *et al.*, 1993). A similar time course as the  
689 IONC-induced change in receptive fields of V2 VPM neurons has also been reported in the  
690 somatosensory cortex after sciatic nerve transection in rats (Wall and Cusick, 1984; Pearson  
691 *et al.*, 1999) and median nerve transection in adult monkeys (Merzenich *et al.*, 1983). Thus,  
692 the somatotopic reorganization in the thalamus induced by the peripheral sensory nerve injury  
693 may in turn influence large-scale receptive field changes in the somatosensory cortex  
694 observed years after dorsal root lesion (Pons *et al.*, 1991; Jones, 2000). The consistency  
695 among our neuroanatomical and behavioral results strongly suggests that the thalamic circuit  
696 remodeling mediating somatotopic reorganization, changes in thalamic receptive fields, and  
697 mechanical hypersensitivity occur within a series of processes that are interdependent.

698 In addition to the general spatial and temporal consistency on our data leading to  
699 above conclusion, it is worthwhile to note that there were several changes of our data along

700 postoperative period. First, ectopic receptive fields mediated by DCN such as what evoked by  
701 chest stimulation were present until two weeks after IONC but absent over one month after  
702 IONC (Figs. 6 and 7 and Tables 1 and 2). Therefore, after IONC, ectopic DCN-origin  
703 lemniscal fibers seem to invade the deafferented V2 VPM once, and they would then be  
704 eliminated by one month after IONC. Second, there was significant recovery in tdTomato  
705 fluorescence intensity of PrV2-origin lemniscal fibers in the V2 VPM between one month and  
706 three months after IONC although it remained still statistically decreased compared with the  
707 survival-period-matched sham groups (Fig. 7D). It means re-strengthening of once weakened  
708 original whisker-sensory pathway. These changes could be considered as the subsequent  
709 second reorganization after the initial large-scale somatotopic reorganization both mediated  
710 by lemniscal fiber remodeling. In the primary somatosensory cortex of non-human primates  
711 deafferented by chronic dorsal column lesion, reactivation of the original receptive fields  
712 occurs over initial two months (Jain *et al.*, 1997), which is very similar to our results (Fig. 7).  
713 The reactivation is followed by large-scale somatotopic reorganization by invasion of ectopic  
714 face representation in both the primary sensory cortex and the somatosensory thalamus over  
715 six months after the deafferentation (Jain *et al.*, 1997; Jain *et al.*, 2008). Thus, pursuits on  
716 further long term reorganization in our model and comparison with these previous non-human  
717 primate studies would provide fruitful insights of somatotopic reorganization in future studies.  
718

#### 719 *Injury-induced remodeling of the somatotopic pathway in the adult*

720 Because the IONC-induced lemniscal fiber reorganization in the V2 VPM was maintained  
721 into adulthood (Fig. 7) and was induced in both juvenile and adult mice (Fig. 8), we conclude  
722 that there is not a critical time window for this injury-induced lemniscal fiber remodeling.  
723 This is consistent with the results in previous studies showing that injury of the primary  
724 sensory neurons by amputation, dorsal root lesion, or dorsal column lesion induces thalamic

725 anatomical and functional changes in adult human and non-human primates: withdrawal of  
726 lemniscal axons (Graziano and Jones, 2009), and large-scale somatotopic reorganization  
727 (Davis *et al.*, 1998; Jones and Pons, 1998; Florence *et al.*, 2000; Jain *et al.*, 2008). In the  
728 present study, we demonstrated that IONC in the adult resulted in anatomical remodeling  
729 including the invasion of ectopic lemniscal fiber terminals (Fig. 8). Thus, it is expected that  
730 IONC in the adult would also cause large-scale receptive field reorganization and  
731 extraterritorial mechanical hypersensitivity (e.g., data shown in Figs. 6 and 7).

732 In the visual thalamus, there is a critical time window for sensory deprivation-induced  
733 retinogeniculate fiber remodeling. Visual deprivation after P20, induces the remodeling onto a  
734 relay neuron in the visual thalamus of the mouse (Hooks and Chen, 2008). In the VPM,  
735 whisker deprivation within a critical time window (P12–P13) disrupts developmental synapse  
736 elimination (Wang and Zhang, 2008; Zhang *et al.*, 2013). Thus, we conclude that the IONC-  
737 induced lemniscal fiber remodeling demonstrated in our study should rely on other  
738 mechanisms different from these developmental processes in the thalamic circuits.

739

740 *Functional implications of lemniscal fiber remodeling in the somatosensory thalamus after*  
741 *peripheral sensory nerve injury*

742 We observed allodynia-like mechanical hypersensitivity on the uninjured mandibular region  
743 after IONC. Similar extraterritorial pain has been reported in cases of the inferior alveolar  
744 nerve transection and cervical spinal nerve injury in patients and animal models, which cause  
745 abnormal orofacial pain in the uninjured face region (Kobayashi *et al.*, 2011; Renton *et al.*,  
746 2012; Tseng *et al.*, 2012; Okada-Ogawa *et al.*, 2015). It has been proposed that changes of  
747 excitability in the trigeminal ganglion and SpC possibly contribute to this extraterritorial  
748 orofacial pain (Kobayashi *et al.*, 2011; Takeda *et al.*, 2011; Okada-Ogawa *et al.*, 2015).  
749 Currently, it remains unclear how allodynia-like mechanical hypersensitivity develops after

750 IONC. Intra-ganglionic and intra-brain stem functional reorganization might contribute to the  
751 abnormal sensation as these previous studies have proposed. Increased projections from the  
752 SpC to the V2 VPM after IONC might also have some contribution (Fig. 5). In the present  
753 study, both thalamic somatotopic reorganization and emergence of extraterritorial pain  
754 behavior occurred with spatiotemporal consistency, suggesting that somatotopic  
755 reorganization at the thalamic level may also be involved in extraterritorial orofacial pain. On  
756 the other hand, it is widely considered that somatotopic reorganization is an essential element  
757 for phantom referred sensation that can often be induced by tactile stimulation on particular  
758 body parts in the amputees (e.g., tactile stimulation on the face induces abnormal sensations  
759 on the lost arm/fingers) (Ramachandran and Hirstein, 1998). It is thought that peripheral nerve  
760 injury causes a contamination of ectopic afferent information in the somatosensory afferent  
761 pathway; the abnormal mis-match between incoming and outgoing somatotopic information  
762 in the CNS results in distorting perception of own body images, leading to the phantom  
763 sensation (Kew *et al.*, 1997; Davis *et al.*, 1998; Grüsser *et al.*, 2004; Flor *et al.*, 2006). In the  
764 somatosensory thalamus, micro-stimulation of the VPL in the amputees whose thalamic  
765 receptive fields are largely reorganized can induce phantom sensations (Davis *et al.*, 1998).  
766 This result supports the idea that thalamic receptive field of an intact body part expands into  
767 the missing limb region of the thalamus after the loss of limb inputs (Davis *et al.*, 1998) and is  
768 consistent with axonal sprouting of afferent fibers in the somatosensory thalamus including  
769 our own results in the present study (Florence and Kaas, 1995; Sengelaub *et al.*, 1997;  
770 Florence *et al.*, 1998; Jain *et al.*, 2000). Taken together, we propose that remodeling of neural  
771 circuit at thalamic levels could underlie the emergence of abnormal ectopic sensations such as  
772 extraterritorial orofacial pain and phantom referred sensation.

773 **References**

- 774 Arsenault D, Zhang Z-W (2006) Developmental remodelling of the lemniscal synapse in the  
775 ventral basal thalamus of the mouse. *J Physiol* 573:121-132.
- 776 Bechara A, Laumonnerie C, Vilain N, Kratochwil CF, Cankovic V, Maiorano NA,  
777 Kirschmann MA, Ducret S, Rijli FM (2015) *Hoxa2* Selects Barrelette Neuron Identity  
778 and Connectivity in the Mouse Somatosensory Brainstem. *Cell Rep* 13:783-797.
- 779 Darian-Smith C, Gilbert CD (1994) Axonal sprouting accompanies functional reorganization  
780 in adult cat striate cortex. *Nature* 368:737-740.
- 781 Davis KD, Kiss ZH, Luo L, Tasker RR, Lozano AM, Dostrovsky JO (1998) Phantom  
782 sensations generated by thalamic microstimulation. *Nature* 391:385-387.
- 783 Faul F, Erdfelder E, Lang AG, Buchner A (2007) G\*Power 3: a flexible statistical power  
784 analysis program for the social, behavioral, and biomedical sciences. *Behav Res*  
785 *Methods* 39:175-191.
- 786 Flor H, Nikolajsen L, Staehelin Jensen T (2006) Phantom limb pain: a case of maladaptive  
787 CNS plasticity? *Nat Rev Neurosci* 7:873-881.
- 788 Flor H, Elbert T, Knecht S, Wienbruch C, Pantev C, Birbaumer N, Larbig W, Taub E (1995)  
789 Phantom-limb pain as a perceptual correlate of cortical reorganization following arm  
790 amputation. *Nature* 375:482-484.
- 791 Florence SL, Kaas JH (1995) Large-scale reorganization at multiple levels of the  
792 somatosensory pathway follows therapeutic amputation of the hand in monkeys. *J*  
793 *Neurosci* 15:8083-8095.
- 794 Florence SL, Taub HB, Kaas JH (1998) Large-scale sprouting of cortical connections after  
795 peripheral injury in adult macaque monkeys. *Science* 282:1117-1121.
- 796 Florence SL, Hackett TA, Strata F (2000) Thalamic and cortical contributions to neural  
797 plasticity after limb amputation. *J Neurophysiol* 83:3154-3159.

- 798 Franklin KBJ, Paxinos G (2008) *The Mouse Brain in Stereotaxic Coordinates*, 3rd Edition.  
799 San Diego: Academic Press.
- 800 Freedman G, Fattal R (2011) Image and video upscaling from local self-examples. *ACM*  
801 *Transactions on Graphics (TOG)* 30:1-11.
- 802 Friedberg MH, Lee SM, Ebner FF (1999) Modulation of receptive field properties of thalamic  
803 somatosensory neurons by the depth of anesthesia. *J Neurophysiol* 81:2243-2252.
- 804 Garraghty PE, Kaas JH (1991) Functional reorganization in adult monkey thalamus after  
805 peripheral nerve injury. *Neuroreport* 2:747-750.
- 806 Glantz SA (2011) *Primer of Biostatistics*, 7th Edition. New York: McGraw-Hill.
- 807 Graziano A, Jones EG (2009) Early withdrawal of axons from higher centers in response to  
808 peripheral somatosensory denervation. *J Neurosci* 29:3738-3748.
- 809 Graziano A, Liu X-B, Murray KD, Jones EG (2008) Vesicular glutamate transporters define  
810 two sets of glutamatergic afferents to the somatosensory thalamus and two  
811 thalamocortical projections in the mouse. *J Comp Neurol* 507:1258-1276.
- 812 Grüsser SM, Winter C, Mühlnickel W, Denke C, Karl A, Villringer K, Flor H (2001) The  
813 relationship of perceptual phenomena and cortical reorganization in upper extremity  
814 amputees. *Neuroscience* 102:263-272.
- 815 Grüsser SM, Mühlnickel W, Schaefer M, Villringer K, Christmann C, Koeppel C, Flor H  
816 (2004) Remote activation of referred phantom sensation and cortical reorganization in  
817 human upper extremity amputees. *Exp Brain Res* 154:97-102.
- 818 Honda Y, Sasaki H, Umitsu Y, Ishizuka N (2012) Zonal distribution of perforant path cells in  
819 layer III of the entorhinal area projecting to CA1 and subiculum in the rat. *Neurosci*  
820 *Res* 74:200-209.
- 821 Hooks BM, Chen C (2008) Vision triggers an experience-dependent sensitive period at the  
822 retinogeniculate synapse. *J Neurosci* 28:4807-4817.

- 823 Iwasato T, Nomura R, Ando R, Ikeda T, Tanaka M, Itohara S (2004) Dorsal telencephalon-  
824 specific expression of Cre recombinase in PAC transgenic mice. *Genesis* 38:130-138.
- 825 Jain N, Catania KC, Kaas JH (1997) Deactivation and reactivation of somatosensory cortex  
826 after dorsal spinal cord injury. *Nature* 386:495-498.
- 827 Jain N, Florence SL, Qi H-X, Kaas JH (2000) Growth of new brainstem connections in adult  
828 monkeys with massive sensory loss. *Proc Natl Acad Sci U S A* 97:5546-5550.
- 829 Jain N, Qi H-X, Collins CE, Kaas JH (2008) Large-scale reorganization in the somatosensory  
830 cortex and thalamus after sensory loss in macaque monkeys. *J Neurosci* 28:11042-  
831 11060.
- 832 Jones EG (2000) Cortical and subcortical contributions to activity-dependent plasticity in  
833 primate somatosensory cortex. *Annu Rev Neurosci* 23:1-37.
- 834 Jones EG, Pons TP (1998) Thalamic and brainstem contributions to large-scale plasticity of  
835 primate somatosensory cortex. *Science* 282:1121-1125.
- 836 Kaas JH, Qi HX, Burish MJ, Gharbawie OA, Onifer SM, Massey JM (2008) Cortical and  
837 subcortical plasticity in the brains of humans, primates, and rats after damage to  
838 sensory afferents in the dorsal columns of the spinal cord. *Exp Neurol* 209:407-416.
- 839 Kakizawa S, Miyazaki T, Yanagihara D, Iino M, Watanabe M, Kano M (2005) Maintenance  
840 of presynaptic function by AMPA receptor-mediated excitatory postsynaptic activity  
841 in adult brain. *Proc Natl Acad Sci U S A* 102:19180-19185.
- 842 Kew JJ, Halligan PW, Marshall JC, Passingham RE, Rothwell JC, Ridding MC, Marsden CD,  
843 Brooks DJ (1997) Abnormal access of axial vibrotactile input to deafferented  
844 somatosensory cortex in human upper limb amputees. *J Neurophysiol* 77:2753-2764.
- 845 Kim SK, Nabekura J (2011) Rapid synaptic remodeling in the adult somatosensory cortex  
846 following peripheral nerve injury and its association with neuropathic pain. *J Neurosci*  
847 31:5477-5482.

- 848 Kis Z, Farkas T, Rábl K, Kis E, Kóródi K, Simon L, Marusin I, Rojik I, Toldi J (1999)  
849 Comparative study of the neuronal plasticity along the neuraxis of the vibrissal  
850 sensory system of adult rat following unilateral infraorbital nerve damage and  
851 subsequent regeneration. *Exp Brain Res* 126:259-269.
- 852 Kobayashi A, Shinoda M, Sessle BJ, Honda K, Imamura Y, Hitomi S, Tsuboi Y, Okada-  
853 Ogawa A, Iwata K (2011) Mechanisms involved in extraterritorial facial pain  
854 following cervical spinal nerve injury in rats. *Mol Pain* 7:12.
- 855 Kobayashi Y, Sano Y, Vannoni E, Goto H, Suzuki H, Oba A, Kawasaki H, Kanba S, Lipp HP,  
856 Murphy NP, Wolfer DP, Itohara S (2013) Genetic dissection of medial habenula-  
857 interpeduncular nucleus pathway function in mice. *Front Behav Neurosci* 7:17.
- 858 Kohno T, Moore KA, Baba H, Woolf CJ (2003) Peripheral nerve injury alters excitatory  
859 synaptic transmission in lamina II of the rat dorsal horn. *J Physiol* 548:131-138.
- 860 Liu X-B, Honda CN, Jones EG (1995) Distribution of four types of synapse on  
861 physiologically identified relay neurons in the ventral posterior thalamic nucleus of the  
862 cat. *J Comp Neurol* 352:69-91.
- 863 Madisen L, Zwingman TA, Sunkin SM, Oh SW, Zariwala HA, Gu H, Ng LL, Palmiter RD,  
864 Hawrylycz MJ, Jones AR, Lein ES, Zeng H (2010) A robust and high-throughput Cre  
865 reporting and characterization system for the whole mouse brain. *Nat Neurosci*  
866 13:133-140.
- 867 Matthews MA, Faciane CL (1977) Electron microscopy of the development of synaptic  
868 patterns in the ventrobasal complex of the rat. *Brain Res* 135:197-215.
- 869 Merzenich MM, Kaas JH, Wall JT, Sur M, Nelson RJ, Felleman DJ (1983) Progression of  
870 change following median nerve section in the cortical representation of the hand in  
871 areas 3b and 1 in adult owl and squirrel monkeys. *Neuroscience* 10:639-665.

- 872 Merzenich MM, Nelson RJ, Stryker MP, Cynader MS, Schoppmann A, Zook JM (1984)  
873 Somatosensory cortical map changes following digit amputation in adult monkeys. *J*  
874 *Comp Neurol* 224:591-605.
- 875 Miura E, Fukaya M, Sato T, Sugihara K, Asano M, Yoshioka K, Watanabe M (2006)  
876 Expression and distribution of JNK/SAPK-associated scaffold protein JSAP1 in  
877 developing and adult mouse brain. *J Neurochem* 97:1431-1446.
- 878 Miyata M, Kashiwadani H, Fukaya M, Hayashi T, Wu D, Suzuki T, Watanabe M, Kawakami  
879 Y (2003) Role of thalamic phospholipase C $\beta$ 4 mediated by metabotropic glutamate  
880 receptor type 1 in inflammatory pain. *J Neurosci* 23:8098-8108.
- 881 Miyazaki T, Fukaya M, Shimizu H, Watanabe M (2003) Subtype switching of vesicular  
882 glutamate transporters at parallel fibre-Purkinje cell synapses in developing mouse  
883 cerebellum. *Eur J Neurosci* 17:2563-2572.
- 884 Navarro X, Vivó M, Valero-Cabré A (2007) Neural plasticity after peripheral nerve injury and  
885 regeneration. *Prog Neurobiol* 82:163-201.
- 886 Nicoletis MAL, Lin RCS, Woodward DJ, Chapin JK (1993) Induction of immediate  
887 spatiotemporal changes in thalamic networks by peripheral block of ascending  
888 cutaneous information. *Nature* 361:533-536.
- 889 Okada-Ogawa A, Nakaya Y, Imamura Y, Kobayashi M, Shinoda M, Kita K, Sessle BJ, Iwata  
890 K (2015) Involvement of medullary GABAergic system in extraterritorial neuropathic  
891 pain mechanisms associated with inferior alveolar nerve transection. *Exp Neurol*  
892 267:42-52.
- 893 Okamoto M, Baba H, Goldstein PA, Higashi H, Shimoji K, Yoshimura M (2001) Functional  
894 reorganization of sensory pathways in the rat spinal dorsal horn following peripheral  
895 nerve injury. *J Physiol* 532:241-250.

- 896 Oury F, Murakami Y, Renaud J-S, Pasqualetti M, Charnay P, Ren S-Y, Rijli FM (2006)  
897 *Hoxa2*- and rhombomere-dependent development of the mouse facial somatosensory  
898 map. *Science* 313:1408-1413.
- 899 Pearson PP, Li CX, Waters RS (1999) Effects of large-scale limb deafferentation on the  
900 morphological and physiological organization of the forepaw barrel subfield (FBS) in  
901 somatosensory cortex (SI) in adult and neonatal rats. *Exp Brain Res* 128:315-331.
- 902 Pons TP, Garraghty PE, Ommaya AK, Kaas JH, Taub E, Mishkin M (1991) Massive cortical  
903 reorganization after sensory deafferentation in adult macaques. *Science* 252:1857-  
904 1860.
- 905 Quiroga RQ, Nadasdy Z, Ben-Shaul Y (2004) Unsupervised spike detection and sorting with  
906 wavelets and superparamagnetic clustering. *Neural comput* 16:1661-1687.
- 907 Ramachandran VS, Hirstein W (1998) The perception of phantom limbs. The D. O. Hebb  
908 lecture. *Brain* 121 ( Pt 9):1603-1630.
- 909 Ren S-Y, Pasqualetti M, Dierich A, Le Meur M, Rijli FM (2002) A *Hoxa2* mutant conditional  
910 allele generated by Flp- and Cre-mediated recombination. *Genesis* 32:105-108.
- 911 Renton T, Dawood A, Shah A, Searson L, Yilmaz Z (2012) Post-implant neuropathy of the  
912 trigeminal nerve. A case series. *Br Dent J* 212:E17.
- 913 Seino H, Seo K, Maeda T, Someya G (2009) Behavioural and histological observations of  
914 sensory impairment caused by tight ligation of the trigeminal nerve in mice. *J*  
915 *Neurosci Methods* 181:67-72.
- 916 Sengelaub DR, Muja N, Mills AC, Myers WA, Churchill JD, Garraghty PE (1997)  
917 Denervation-induced sprouting of intact peripheral afferents into the cuneate nucleus  
918 of adult rats. *Brain Res* 769:256-262.
- 919 Simons DJ (1983) Multi-whisker stimulation and its effects on vibrissa units in rat Sml barrel  
920 cortex. *Brain Res* 276:178-182.

- 921 Takeda M, Tsuboi Y, Kitagawa J, Nakagawa K, Iwata K, Matsumoto S (2011) Potassium  
922 channels as a potential therapeutic target for trigeminal neuropathic and inflammatory  
923 pain. *Mol Pain* 7:5.
- 924 Takeuchi Y, Yamasaki M, Nagumo Y, Imoto K, Watanabe M, Miyata M (2012) Rewiring of  
925 afferent fibers in the somatosensory thalamus of mice caused by peripheral sensory  
926 nerve transection. *J Neurosci* 32:6917-6930.
- 927 Takeuchi Y, Asano H, Katayama Y, Muragaki Y, Imoto K, Miyata M (2014) Large-scale  
928 somatotopic refinement via functional synapse elimination in the sensory thalamus of  
929 developing mice. *J Neurosci* 34:1258-1270.
- 930 Tomasi C, Manduchi R (1998) Bilateral filtering for gray and color images. In: Proceedings  
931 of the 1998 IEEE International Conference on Computer Vision, pp 839-846. Bombay,  
932 India.
- 933 Tseng WT, Tsai ML, Iwata K, Yen CT (2012) Long-term changes in trigeminal ganglionic  
934 and thalamic neuronal activities following inferior alveolar nerve transection in  
935 behaving rats. *J Neurosci* 32:16051-16063.
- 936 Veinante P, Deschênes M (1999) Single- and multi-whisker channels in the ascending  
937 projections from the principal trigeminal nucleus in the rat. *J Neurosci* 19:5085-5095.
- 938 Voiculescu O, Charnay P, Schneider-Maunoury S (2000) Expression pattern of a *Krox-20/Cre*  
939 knock-in allele in the developing hindbrain, bones, and peripheral nervous system.  
940 *Genesis* 26:123-126.
- 941 Waite PM (1984) Rearrangement of neuronal responses in the trigeminal system of the rat  
942 following peripheral nerve section. *J Physiol* 352:425-445.
- 943 Wall JT, Cusick CG (1984) Cutaneous responsiveness in primary somatosensory (S-I)  
944 hindpaw cortex before and after partial hindpaw deafferentation in adult rats. *J*  
945 *Neurosci* 4:1499-1515.

- 946 Wang H, Zhang Z-W (2008) A critical window for experience-dependent plasticity at whisker  
947 sensory relay synapse in the thalamus. *J Neurosci* 28:13621-13628.
- 948 Watson C, Paxinos G, Puelles L (2012) *The mouse nervous system*, 1st Edition. London:  
949 Academic Press.
- 950 Woolf CJ, Mannion RJ (1999) Neuropathic pain: aetiology, symptoms, mechanisms, and  
951 management. *Lancet* 353:1959-1964.
- 952 Yamahachi H, Marik SA, McManus JNJ, Denk W, Gilbert CD (2009) Rapid axonal sprouting  
953 and pruning accompany functional reorganization in primary visual cortex. *Neuron*  
954 64:719-729.
- 955 Yu X, Chung S, Chen D-Y, Wang S, Dodd SJ, Walters JR, Isaac JT, Koretsky AP (2012)  
956 Thalamocortical inputs show post-critical-period plasticity. *Neuron* 74:731-742.
- 957 Zhang Z-W, Peterson M, Liu H (2013) Essential role of postsynaptic NMDA receptors in  
958 developmental refinement of excitatory synapses. *Proc Natl Acad Sci U S A*  
959 110:1095-1100.
- 960

961 **Legends**962 **Figure 1. Transection of infraorbital nerve induced anatomical remodeling in whisker**  
963 **sensory pathway.**

964 **A**, Schematic drawing of genetic visualization of PrV2-origin lemniscal fibers. (**A**<sub>1</sub>): Alleles  
965 of Krox-20<sup>Cre</sup> and Ai14 mouse lines. These lines were crossed. (**A**<sub>2</sub>): Selective labeling of  
966 PrV2-origin lemniscal fibers with tdTomato. Boxed area over the left Pr5 indicates the region  
967 shown in (**C**<sub>2</sub>). Horizontal dotted lines indicate horizontal planes shown in (**C**<sub>1</sub>) and (**D**). **B**,  
968 Experimental schedule of IONC. **C**, tdTomato signals in the PrV2 (**C**<sub>2</sub>) and on the ascending  
969 tract (**C**<sub>1</sub>) did not change after IONC. Scale bar, 200  $\mu$ m. **D**, tdTomato signals in the V2 VPM  
970 of Krox20-Ai14 mice. Arrowheads indicate the affected V2 VPM. Yellow enclosures indicate  
971 automatically detected ROIs for analyses. Scale bar, 500  $\mu$ m. **E**, Ratio of contralateral to  
972 ipsilateral tdTomato signals of the V2 VPM in fluorescent intensity and area. Values are  
973 represented as mean  $\pm$  s.d., eighteen images from nine mice were analyzed for each group.  
974 Statistical significance was tested by two-way repeated measures ANOVA (main effect of  
975 IONC). \*\*\* $P < 0.001$  (main effect of operation); two-tailed. Pr5, principle trigeminal nucleus;  
976 PrV2, maxillary Pr5; V2, maxillary region; V3, mandibular region; VPM, ventral  
977 posteromedial thalamic nucleus.

978

979 **Figure 2. IONC increased non-PrV2-origin lemniscal fiber terminals in V2 VPM related**  
980 **to newly recruited lemniscal fibers onto VPM neurons.**

981 **A**, VGluT2-immunostained V2 VPM sections of Krox20-Ai14 mice. VGluT2 is a marker of  
982 lemniscal fiber terminals in the VPM. Top: Significant increase of tdT-negative (non-PrV2-  
983 origin) VGluT2 puncta in the contralateral V2 VPM after IONC. Scale bar, 20  $\mu$ m. Bottom:  
984 the soma and dendrites of V2 VPM neurons were visualized by fluoro Nissl and MAP2  
985 stainings, respectively, in addition to VGluT2 and tdTomato (top) to examine subcellular

986 distribution of the VGluT2 puncta in their origin-specific manner. \* indicates a V2 VPM  
987 neuron; arrows indicate somatic puncta; arrowheads indicate dendritic puncta. Scale bar, 5  $\mu$ m.  
988 **B**, Summary density of VGluT2 puncta in the V2 VPM. tdT(+) = tdTomato-positive VGluT2;  
989 tdT(-) = tdTomato-negative ones. **C**, IONC decreased proportion of tdT(+) VGluT2 puncta in  
990 the contralateral V2 VPM. **D**, Summary numbers of VGluT2 puncta on the soma (left) and  
991 proximal dendrites (right) in the contralateral V2 VPM. tdT-positive puncta decreased  
992 whereas tdT-negative ones increased both on the soma and dendrites. A marker indicates each  
993 V2 VPM neuron examined. tdT(+) = tdTomato-positive VGluT2; tdT(-) = tdTomato-negative  
994 ones. **E**, Correlated postoperative time course of anatomical and functional lemniscal fiber  
995 remodeling in the V2 VPM. Top: VGluT2-immunostaining. Scale bar, 20  $\mu$ m. Bottom:  
996 Discrete lemniscal fiber-mediated EPSCs in a V2 VPM neuron in response to increasing  
997 electrical stimuli on the medial lemniscal fiber bundle (Takeuchi *et al.*, 2012). **F**, Correlation  
998 between anatomical and functional lemniscal fiber remodeling in the contralateral V2 VPM. *r*,  
999 Pearson's correlation coefficient. Broken line is the regression line. **G**, Experimental schedule  
1000 of whisker deprivation. **H**, VGluT2-immunostained sections of the V2 VPM in Krox20-Ai14  
1001 mice after whisker deprivation. Scale bar, 20 $\mu$ m. **I**, Summary density of VGluT2 puncta in the  
1002 contralateral V2 VPM. tdT(+) = tdTomato-positive VGluT2; tdT(-) = tdTomato-negative ones.  
1003 Values are represented as mean ( $\pm$  s.d.). Three to nine mice (eight images from each mouse)  
1004 were analyzed for each group in (A–I). In total, 94 neurons from four mice (4–10 neurons  
1005 from each image) were analyzed for each group in (D). In total, 215 neurons from 91 mice  
1006 and 118 images from 14 mice were analyzed for (E and F). Statistical significance was tested  
1007 by two-way repeated measures ANOVA (main effect of IONC or whisker deprivation) for  
1008 (B–D, and I) and Pearson's product-moment correlation test for (F). \* $P < 0.05$ ; \*\* $P < 0.01$ ;  
1009 \*\*\* $P < 0.001$ ; n.s., not significant; two-tailed.  
1010

1011 **Figure 3. IONC decreased size of PrV2-origin lemniscal fiber terminals in V2 VPM and**  
1012 **amplitude of lemniscal fiber-derived miniature EPSCs.**

1013 **A**, VGluT2-immunostained V2 VPM sections of Krox20-Ai14 mice. Scale bar, 5  $\mu\text{m}$ . **B**,  
1014 Cumulative probabilities of tdT-positive VGluT2 puncta in the V2 VPM after sham and  
1015 IONC operation. Nine mice (eight images from each mouse) were analyzed for each group. **C**,  
1016 Averaged traces of asynchronously released miniature EPSCs from a lemniscal fiber in the  
1017 VPM. Traces of 1517 and 2356 events from 12 and 15 neurons of sham- and IONC-operated  
1018 mice, respectively. **D**, Cumulative probabilities of lemniscal fiber-derived miniature EPSC  
1019 amplitude. Statistical significance was tested by two-sample Kolmogorov-Smirnov test for (B  
1020 and D). \*\*\* $P < 0.001$ ; two-tailed.

1021

1022 **Figure 4. IONC induced morphological changes of PrV2-origin lemniscal fibers in V2**  
1023 **VPM.**

1024 **A**, BDA, an anterograde neural tracer, was injected in the left PrV2. **B**, PrV2-origin lemniscal  
1025 fibers in the contralateral V2 VPM. Scale bar, 10  $\mu\text{m}$ . **C–E**, Projection images of 3-D  
1026 reconstructed terminal morphology of single PrV2-origin lemniscal fibers ( $C_1$ ,  $D_1$ , and  $E_1$ )  
1027 and their quantitative analyses ( $C_2$ ,  $D_2$ , and  $E_2$ ). **C**, Scale bar, 50  $\mu\text{m}$ . **D**, Ectopic branches  
1028 were defined as branches over 50  $\mu\text{m}$  away from the barycenter of boutons. **E**, Distances  
1029 between all pairs of boutons and terminals in each PrV2-origin fiber were analyzed. Values  
1030 are represented as mean  $\pm$  s.d. A marker indicates each fiber for ( $C_2$ ) and ( $D_2$  left). Twenty-  
1031 one and 44 fibers from three mice were analyzed for sham and IONC groups, respectively.  
1032 Statistical significance was tested by two-way repeated measures ANOVA (main effect of  
1033 IONC) for ( $C_2$ ) and ( $D_2$  left) and two-sample Kolmogorov-Smirnov test for ( $D_2$  right) and  
1034 ( $E_2$ ). \*\* $P < 0.01$ ; \*\*\* $P < 0.001$ ; two-tailed.

1035

1036 **Figure 5. IONC induced lemniscal fiber innervations from non-V2 brain stem nuclei to**  
1037 **V2 VPM.**

1038 **A**, A solution containing cholera toxin B subunit (CTB), an efficient neural tracer, was  
1039 injected in the right V2 VPM of sham (left)- or IONC (right)-operated Krox20-Ai14 mice to  
1040 retrogradely label projection neurons terminating the V2 VPM. Injection sites of analyzed  
1041 mice were reconstructed as green enclosures in the brain atlas of Franklin and Paxinos (2008).  
1042 Injection sites shown as pictures were depicted by thick lines. Scale bars, 400  $\mu\text{m}$ . **B**,  
1043 Retrogradely labeled neurons in the V2 and V3 regions of the Pr5 in sham (left) and IONC  
1044 (right). *See Materials and Methods* for details regarding identification of V2 and V3 regions.  
1045 Cytochrome oxidase (CO)-stained adjacent sections are also shown ( $B_1$ , leftmost). Squared  
1046 regions in  $B_1$  are magnified in  $B_2$ . Scale bars for low ( $B_1$ ) and high ( $B_2$ ) magnifications, 400  
1047  $\mu\text{m}$  and 100  $\mu\text{m}$ , respectively. **C**, Retrogradely-labeled neurons in the interpolar subnucleus of  
1048 the spinal trigeminal nuclei (SpI), and the dorsal column nuclei (DCN) in sham (left) and  
1049 IONC (right). CTB-immunofluorescence of squared regions is magnified in the rightmost and  
1050 CO-stained adjacent sections are also shown (leftmost). Scale bars for low and high  
1051 magnifications, 400  $\mu\text{m}$  and 100  $\mu\text{m}$ . Cu, cuneate nucleus; Gr, gracile nucleus. **D**, Summary  
1052 bar graph showing numbers of retrogradely-labeled neurons from the V2 VPM. Values are  
1053 represented as mean  $\pm$  s.d. Three and four mice (four ROIs of separate sections from each  
1054 animal) were examined for sham and IONC groups, respectively. Statistical significance was  
1055 tested by two-way repeated measures ANOVA (main effect of IONC). \*\*\* $P < 0.001$ ; n.s., not  
1056 significant; two-tailed. **E**, Nissl- and CO-stained adjacent brain stem sections of an IONC-  
1057 operated mouse showing Cu and the caudal subnucleus of the spinal trigeminal nuclei (SpC)  
1058 in the ipsilateral side of IONC. Clear cyto-architecture was retained; there is no collapse of  
1059 boundaries between Cu and SpC. Mx, matrix region of the medulla. Scale bar, 400  $\mu\text{m}$ .  
1060

1061 **Figure 6. IONC induced ectopic receptive fields of V2 VPM neurons and mechanical**  
1062 **hypersensitivities on mandibular region of face.**

1063 **A, C,** Recording sites located by electrical lesion made after receptive field recordings. Only  
1064 recordings in the V2 VPM characterized by dense tdTomato-labeled lemniscal fiber terminals  
1065 were analyzed. A representative image is shown (A) and all recording sites analyzed were  
1066 reconstructed in the brain atlas of Franklin and Paxinos (2008) (C). Black circles = recording  
1067 sites of maxillary receptive fields only; Blue circles = recording sites of mandibular receptive  
1068 fields; Red circles = recording sites of non-trigeminal receptive fields; Magenta circles =  
1069 recording sites of both mandibular and non-trigeminal receptive fields; Multiplication signs =  
1070 non-responsive sites. Magenta brackets indicate the manually traced V2 VPM regions. Roman  
1071 numerals indicate recording sites of representative recordings shown in (B) and (D). Scale  
1072 bars, 1 mm. Cx, cerebral cortex; Hip, hippocampus; VPM, ventral posteromedial thalamic  
1073 nucleus. **B,** Representative recording of IONC-operated mouse at the recording site (iii). Red  
1074 vertical line indicates the timing of cue for stimulation. Time scale, 250 ms; Scale for  
1075 peristimulus time histogram, 10 spikes. **D,** Representative receptive fields of V2 VPM  
1076 neurons. Each Roman numeral corresponds to the recording from the site indicated in (C).  
1077 Colored areas on the age-matched mouse traces indicate receptive fields at the recording sites.  
1078 Magenta = sham; green = IONC. Body surface at which there is stimulus-locked significant  
1079 increase in firing rate from basal firing is considered as the receptive field. **E,** Face-escape  
1080 thresholds assessed by von Frey filament stimuli on whisker pad and lower jaw before and 1–  
1081 15 days after IONC operation on P21. Each value was normalized to that of sham group.  
1082 Twelve mice for each group were examined. Values are represented as mean  $\pm$  s.d. Statistical  
1083 significance was tested by two-way repeated ANOVA and *post-hoc* Tukey HSD test. \* $P <$   
1084 0.05; \*\* $P <$  0.01; n.s., not significant; two-tailed.

1085

1086 **Figure 7. Long-lasting lemniscal fiber remodeling related to ectopic receptive fields of**  
1087 **V2 VPM neurons and mechanical hypersensitivities on ectopic receptive fields.**  
1088 **A**, Experimental schedule. **B**, tdTomato signals in the V2 VPM of Krox20-Ai14 mice long  
1089 after IONC. Arrowheads indicate the affected V2 VPM. Scale bar, 500  $\mu$ m. **C**, VGluT2-  
1090 immunostained sections of the V2 VPM. Significant increases of tdT-negative VGluT2  
1091 puncta after IONC. Scale bar, 20  $\mu$ m. **D**, Ratios of contralateral to ipsilateral tdTomato signals  
1092 of the V2 VPM in fluorescent intensity and area. Four mice (four images from each mouse)  
1093 were examined for each group. **E**, Summary density of VGluT2 puncta in the contralateral V2  
1094 VPM. tdT(+) = tdTomato-positive VGluT2; tdT(-) = tdTomato-negative ones. **F**, IONC  
1095 decreased proportion of tdT-positive VGluT2 puncta in the contralateral V2 VPM. Four mice  
1096 (eight images from each mouse) were examined for each group in (E) and (F). **G**, Recording  
1097 sites located by electrical lesion made after receptive field recordings. All recordings made in  
1098 the V2 VPM were analyzed and reconstructed in the brain atlas of Franklin and Paxinos  
1099 (2008). Black circles = recording sites of maxillary receptive fields only; Blue circles =  
1100 recording sites of mandibular receptive fields; Multiplication signs = non-responsive sites.  
1101 Magenta brackets indicate the V2 VPM regions. Roman numerals indicate the recording sites  
1102 of representative recordings shown in (H). Scale bar, 1 mm. **H**, Representative receptive fields  
1103 of V2 VPM neurons. Each Roman numeral corresponds to the recording from the site  
1104 indicated in (G). Colored areas on the mouse cartoons indicate receptive fields at the  
1105 recording sites. Magenta = sham; green = IONC. **I**, Face-escape thresholds assessed by von  
1106 Frey filament stimuli on whisker pad and lower jaw before and 0.5–4.5 months after IONC  
1107 operation on P21. Nerve regeneration was prevented for long-term evaluation (*see Materials*  
1108 *and Methods*). Each value was normalized to that of the sham group. Nine mice were  
1109 examined for each group. Values are represented as mean  $\pm$  s.d. Statistical significance was  
1110 tested by two-way repeated measures ANOVA (main effect of IONC) for (D–F) and two-way

1111 repeated measures ANOVA and *post-hoc* Tukey HSD test for (I). \* $P < 0.05$ ; \*\* $P < 0.01$ ;  
1112 \*\*\* $P < 0.001$ ; two-tailed.

1113

1114 **Figure 8. No critical window of IONC-induced lemniscal fiber remodeling.**

1115 **A**, IONC operation was conducted on adult Krox20-Ai14 mice. **B**, tdTomato signals in the V2  
1116 VPM of Krox20-Ai14 mice IONC-operated in adult. Arrowheads indicate the affected  
1117 thalamus. Scale bar, 500  $\mu\text{m}$ . **C**, Ratios of contralateral to ipsilateral tdTomato signals of the  
1118 V2 VPM in fluorescent intensity and area. Sixteen images from five mice were examined for  
1119 each group. **D**, VGluT2-immunostained sections of the contralateral V2 VPM in Krox20-Ai14  
1120 mice IONC-operated in adult. Scale bar, 20 $\mu\text{m}$ . **E**, Summary density of VGluT2 puncta in the  
1121 V2 VPM. tdT(+) = tdTomato-positive VGluT2; tdT(-) = tdTomato-negative ones. **F**,  
1122 Summary proportion of tdT-positive VGluT2 in the V2 VPM. Three mice (eight images from  
1123 each mouse) were examined for each group in (E) and (F). Values are represented as mean  $\pm$   
1124 s.d. Statistical significance was tested by two-way repeated measures ANOVA (main effect of  
1125 IONC) for (C, E, and F). \* $P < 0.05$ ; \*\*\* $P < 0.001$ ; n.s., not significant; two-tailed.

1126

1127 **Table 1. Receptive fields of V2 VPM neurons one to two-weeks after operations.**

1128 Recordings were made from the right V2 VPM. All receptive fields (RFs) were found in the  
1129 contralateral (left) side of the face and/or body. For the sham group, 42 recording sites were  
1130 mapped from six mice (six penetrations) in total. For the IONC group, 65 recording sites were  
1131 mapped from five mice (seven penetrations) in total. Note that in several cases each recording  
1132 site had multiple RFs such as the lower jaw and the chest. DCN, dorsal column nuclei; IONC,  
1133 infraorbital nerve cut; PrV2, maxillary region of the principle trigeminal nucleus; PrV3,  
1134 mandibular region of the principle trigeminal nucleus; V2 SpI, maxillary region of the

1135 interpolar subnucleus of the spinal trigeminal nuclei; V3 SpI, mandibular region of the  
1136 interpolar subnucleus of the spinal trigeminal nuclei.

1137

1138 **Table 2. Receptive fields of V2 VPM neurons one to three-months after operations.**

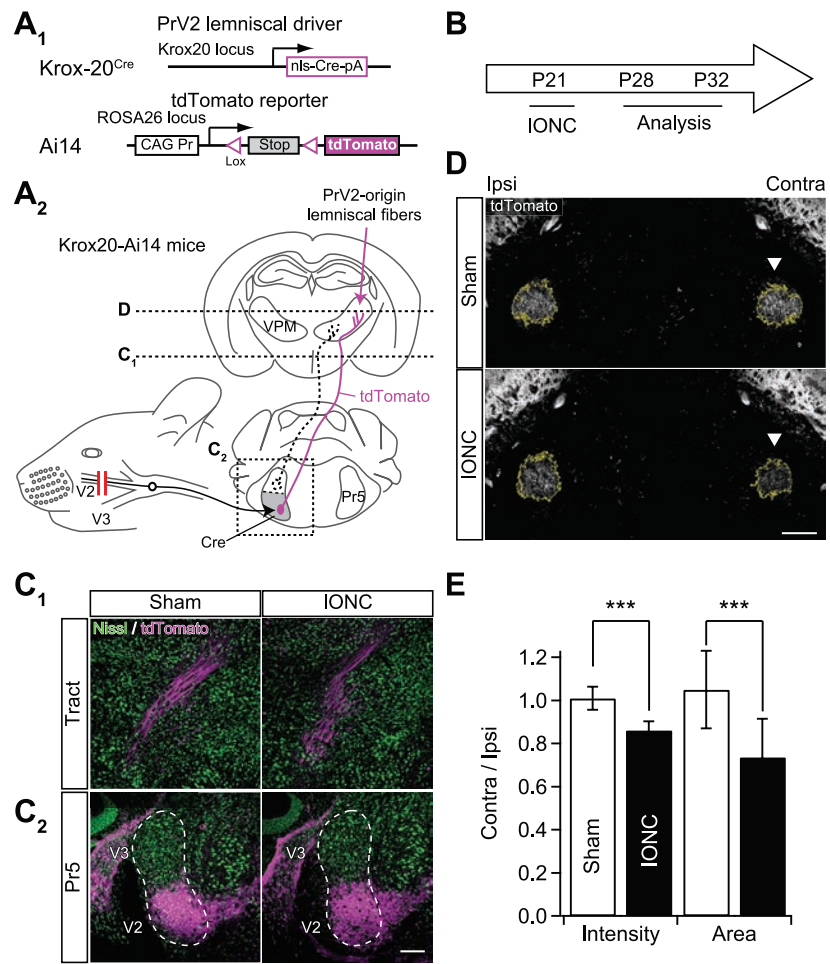
1139 Recordings were made from the right V2 VPM. All receptive fields (RFs) were found in the  
1140 contralateral (left) side of the face and/or body. For the sham group, 21 recording sites were  
1141 mapped from three mice (three penetrations) in total. For the IONC group, 52 recording sites  
1142 were mapped from three mice (five penetrations) in total. Note that in several cases each  
1143 recording site had multiple RFs such as the lower jaw and the whisker pad. IONC, infraorbital  
1144 nerve cut; PrV2, maxillary region of the principle trigeminal nucleus; PrV3, mandibular  
1145 region of the principle trigeminal nucleus; V2 SpI, maxillary region of the interpolar  
1146 subnucleus of the spinal trigeminal nuclei; V3 SpI, mandibular region of the interpolar  
1147 subnucleus of the spinal trigeminal nuclei.

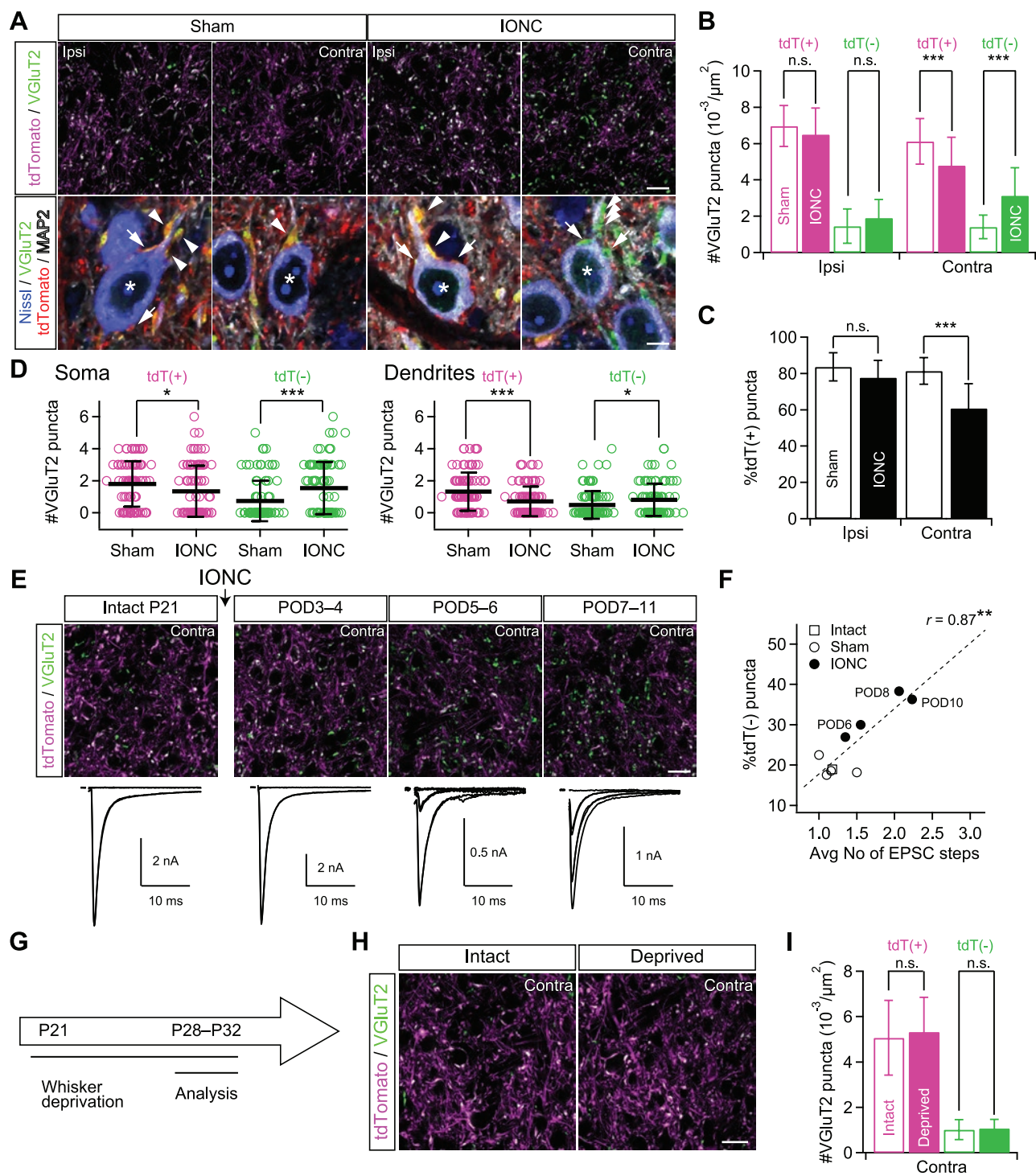
1148

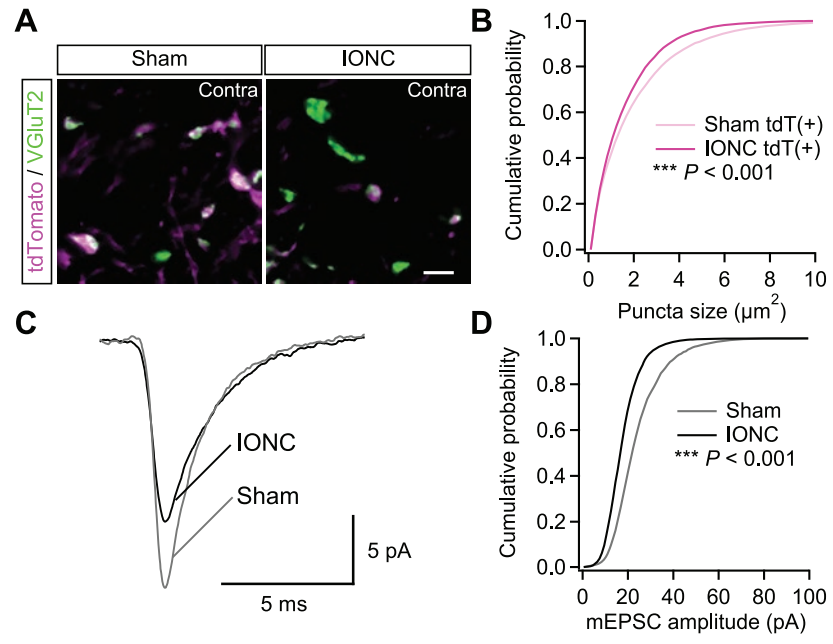
1149 **Table 3. Statistical tests**

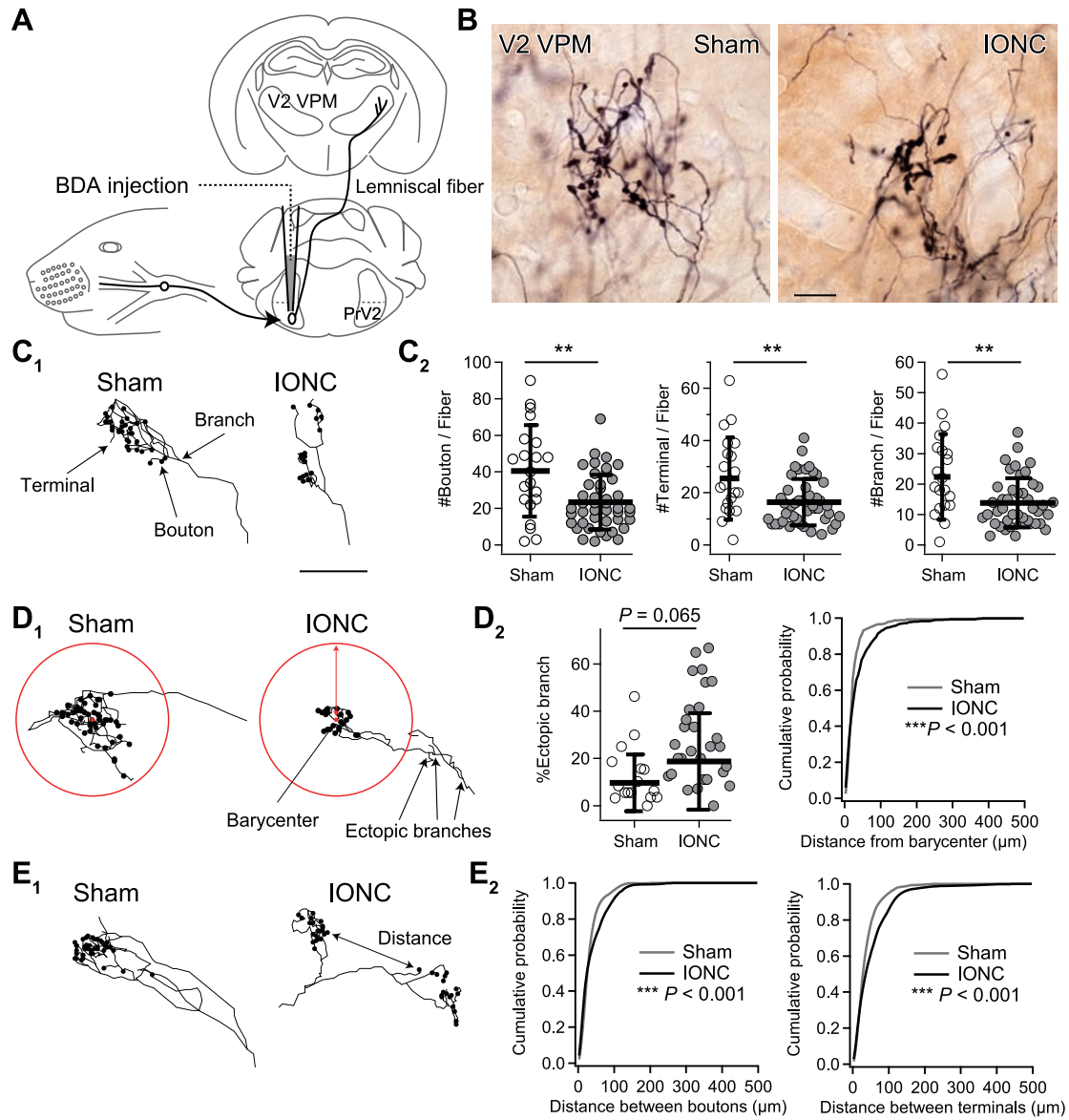
1150 Each small alphabetical character indicates statistical tests labeled with a *p*-value and the  
1151 small alphabetical character in the Result section. Data normality was determined using the  
1152 Lilliefors test. Nonparametric statistical analysis produced similar results. *Post-hoc* power  
1153 analysis was performed using G\*Power 3 software (Faul et al., 2007). *Post-hoc* powers of  
1154 two-way repeated measures ANOVA were calculated on main effect of operation (IONC or  
1155 whisker deprivation) except w and x (main effect of survival period). n.a., not applicable; *p*-  
1156 values were provided instead.

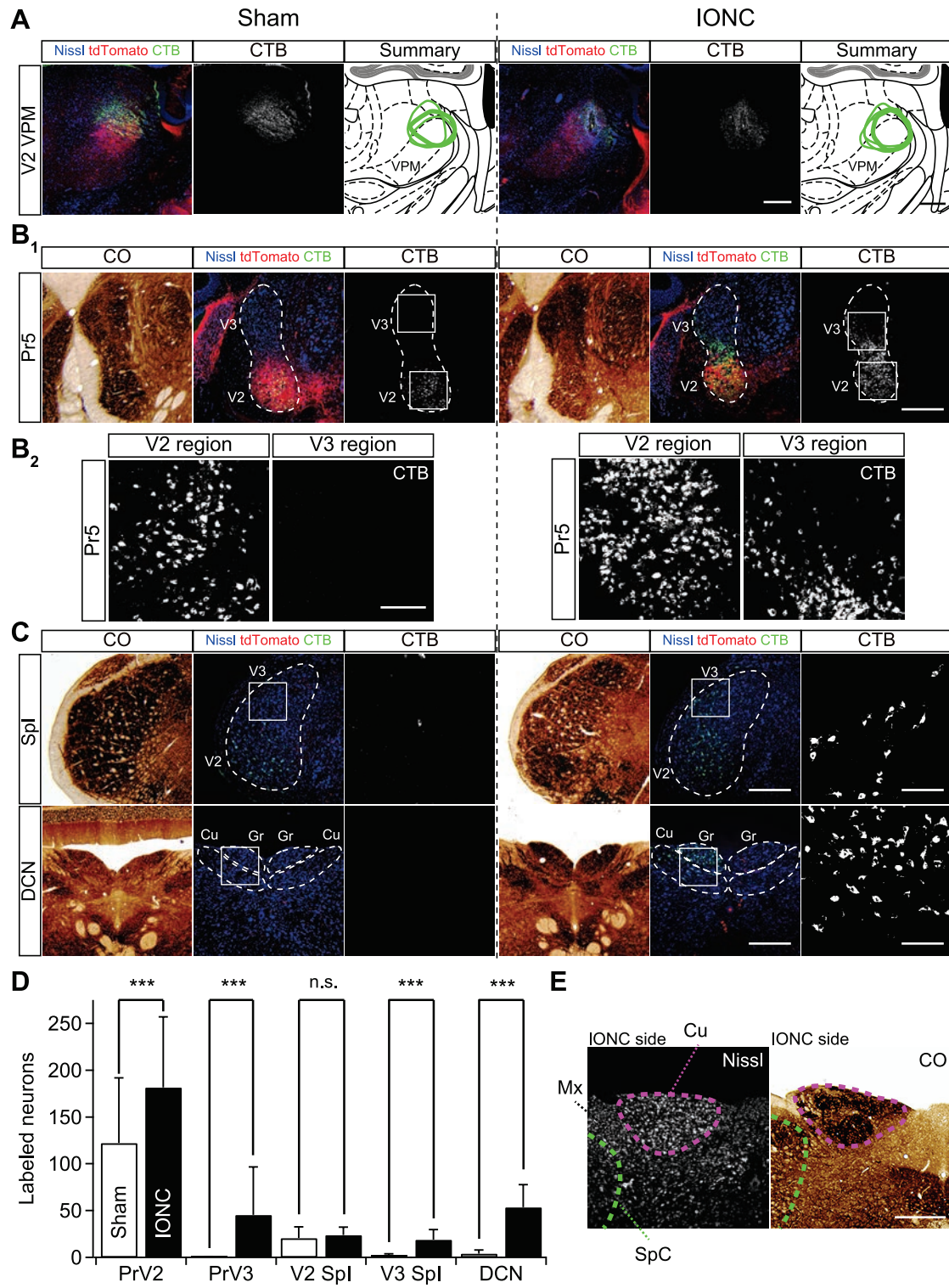
1157

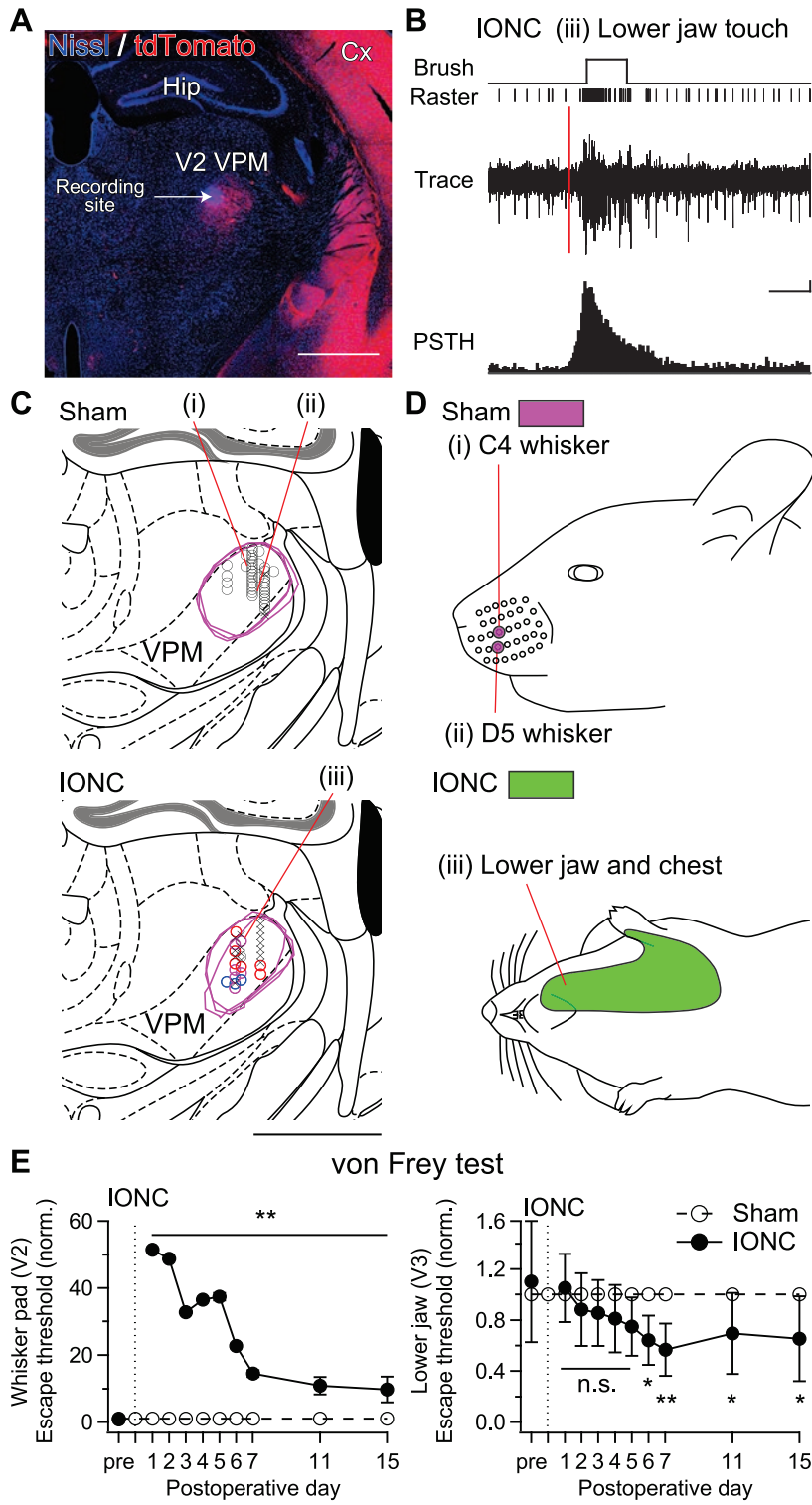


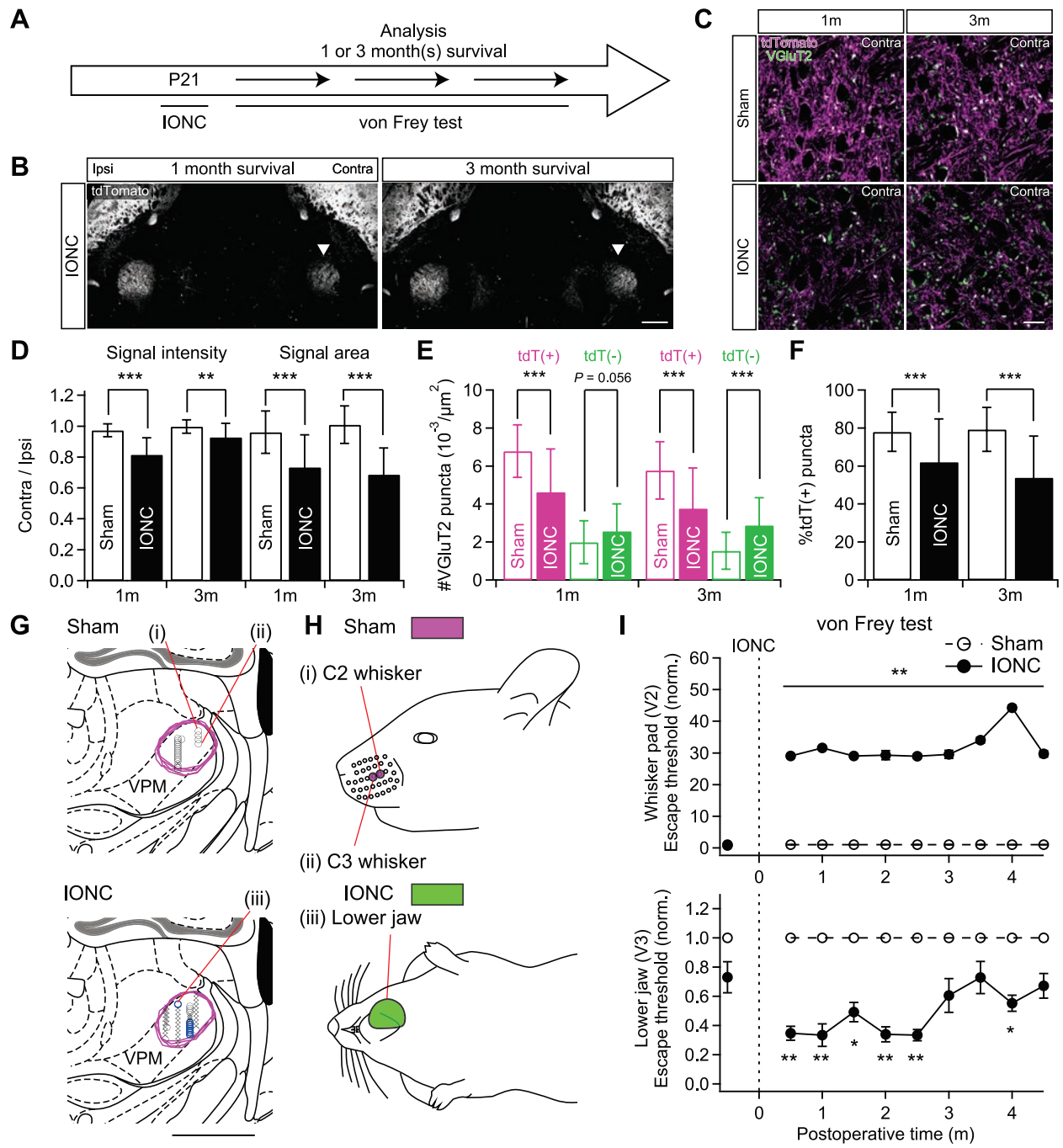


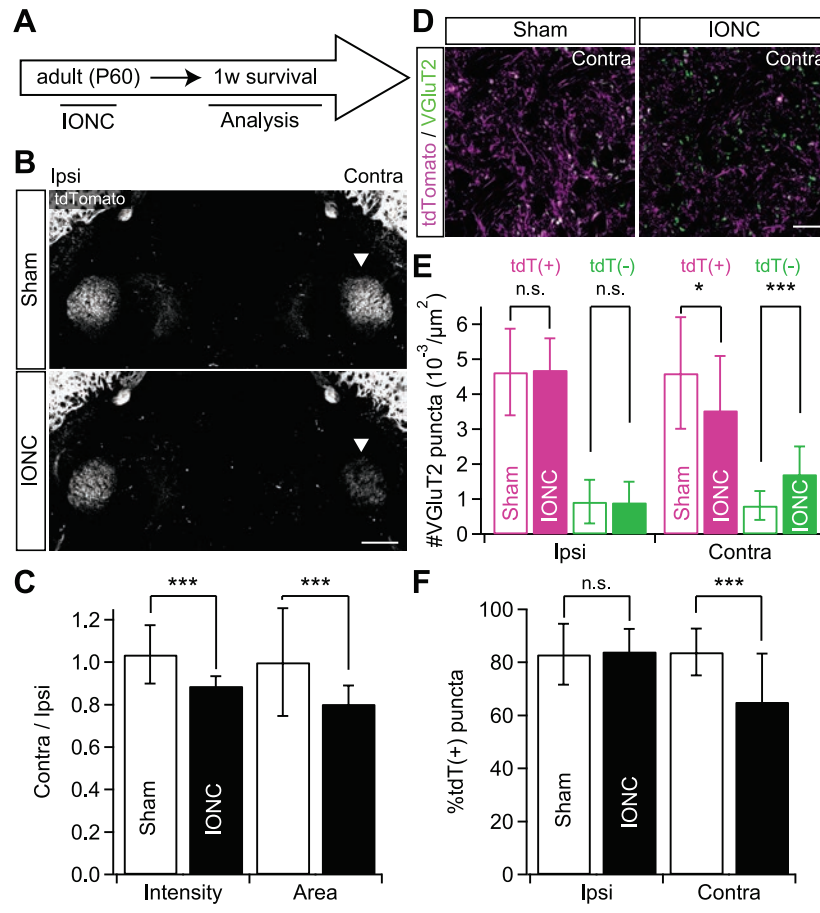












Operation	RF location	Corresponding brain stem nuclei	Number of recordings	Proportion to total mapped sites (%)
Sham	Whisker(s) or whisker pad	PrV2, V2 SpI	39	92.9
	Non-responsive	none	3	7.1
IONC	Whisker(s) or whisker pad	PrV2, V2 SpI	3	4.6
	Lower jaw	PrV3, V3 SpI	9	13.8
	Chest	DCN	6	9.2
	Fore paw	DCN	3	4.6
	Hind paw	DCN	1	1.5
	Trunk	DCN	1	1.5
	Tail	DCN	1	1.5
	Non-responsive	none	50	76.9

Table 1

Operation	RF location	Corresponding brain stem nuclei	Number of recordings	Proportion to total mapped sites (%)
Sham	Whisker(s) or whisker pad	PrV2, V2 SpI	20	95.2
	Non-responsive	none	1	4.8
IONC	Whisker(s) or whisker pad	PrV2, V2 SpI	7	13.5
	Lower jaw	PrV3, V3 SpI	8	15.4
	Non-responsive	none	38	73.1

Table 2

	Data structure	Type of test	Power ( $\alpha = 0.05$ )
a (Fig. 1E, intensity)	Normal	Two-way repeated measures ANOVA	1.0000000
a (Fig. 1E, area)	Normal	Two-way repeated measures ANOVA	1.0000000
b [Fig. 2B, tdT(+)]	Normal	Two-way repeated measures ANOVA	1.0000000
c [Fig. 2B, tdT(-)]	Unknown	Two-way repeated measures ANOVA	1.0000000
d	Normal	Two-way repeated measures ANOVA	0.9786688
e (Fig. 2C)	Normal	Two-way repeated measures ANOVA	1.0000000
f [Fig. 2D, soma, tdT(+)]	Unknown	Two-way repeated measures ANOVA	1.0000000
f [Fig. 2D, dendrites, tdT(+)]	Unknown	Two-way repeated measures ANOVA	1.0000000
g [Fig. 2D, soma, tdT(-)]	Unknown	Two-way repeated measures ANOVA	1.0000000
g [Fig. 2D, dendrites, tdT(-)]	Unknown	Two-way repeated measures ANOVA	1.0000000
h	Unknown	Pearson's $\chi^2$ test	0.8460473
i (Fig. 2F)	Unknown	<i>t</i> -test for non-correlation	0.9759325
j [Fig. 2I, tdT(+)]	Normal	Two-way repeated measures ANOVA	0.2974602
j [Fig. 2I, tdT(-)]	Normal	Two-way repeated measures ANOVA	0.1588404
j [%tdT(+)]	Unknown	Two-way repeated measures ANOVA	0.2390769
k	Unknown	Two-way repeated measures ANOVA	1.0000000
l (Fig. 3B)	Unknown	Kolmogorov-Smirnov two-sample test	n.a. ( $p = 5.5 \times 10^{-28}$ )
m	Normal	Two-way repeated measures ANOVA	0.1673505
n (Fig. 3D)	Unknown	Kolmogorov-Smirnov two-sample test	n.a. ( $p = 9.0 \times 10^{-83}$ )
o (Fig. 4C <sub>2</sub> , Bouton)	Normal	Two-way repeated measures ANOVA	1.0000000
o (Fig. 4C <sub>2</sub> , Terminal)	Normal	Two-way repeated measures ANOVA	1.0000000
o (Fig. 4C <sub>2</sub> , Branch)	Normal	Two-way repeated measures ANOVA	1.0000000
p (Fig. 4D <sub>2</sub> right)	Unknown	Kolmogorov-Smirnov two-sample test	n.a. ( $p = 1.7 \times 10^{-7}$ )
q (Fig. 4D <sub>2</sub> left)	Unknown	Two-way repeated measures ANOVA	0.9999438
r (Fig. 4E <sub>2</sub> left)	Unknown	Kolmogorov-Smirnov two-sample test	n.a. ( $p = 2.7 \times 10^{-148}$ )
r (Fig. 4E <sub>2</sub> right)	Unknown	Kolmogorov-Smirnov two-sample test	n.a. ( $p = 2.7 \times 10^{-115}$ )
s (Fig. 5D, PrV2)	Normal	Two-way repeated measures ANOVA	1.0000000
s (Fig. 5D, PrV3)	Unknown	Two-way repeated measures ANOVA	1.0000000

s (Fig. 5D, V2 Spl)	Normal	Two-way repeated measures ANOVA	0.9465853
s (Fig. 5D, V3 Spl)	Normal	Two-way repeated measures ANOVA	1.0000000
s (Fig. 5D, DCN)	Normal	Two-way repeated measures ANOVA	1.0000000
t	Unknown	Two-way repeated measures ANOVA	1.0000000
u (Fig. 6E right)	Normal	Two-way repeated measures ANOVA	0.8840900
v (Fig. 7D, 1m intensity)	Normal	Two-way repeated measures ANOVA	1.0000000
v (Fig. 7D, 1m area)	Normal	Two-way repeated measures ANOVA	1.0000000
v (Fig. 7D, 3m intensity)	Normal	Two-way repeated measures ANOVA	1.0000000
v (Fig. 7D, 3m area)	Normal	Two-way repeated measures ANOVA	1.0000000
w	Normal	Two-way repeated measures ANOVA	1.0000000
x	Normal	Two-way repeated measures ANOVA	0.5385280
y [Fig. 7E, 3m, tdT(+)]	Normal	Two-way repeated measures ANOVA	1.0000000
z [Fig. 7E, 3m, tdT(-)]	Normal	Two-way repeated measures ANOVA	1.0000000
aa [Fig. 7F, 3m, %tdT(+)]	Normal	Two-way repeated measures ANOVA	1.0000000
bb (Fig. 7I bottom)	Normal	Two-way repeated measures ANOVA	1.0000000
cc (Fig. 8C, intensity)	Normal	Two-way repeated measures ANOVA	1.0000000
cc (Fig. 8C, area)	Normal	Two-way repeated measures ANOVA	1.0000000
dd [Fig. 8E, tdT(+)]	Normal	Two-way repeated measures ANOVA	1.0000000
ee [Fig. 8E, tdT(-)]	Normal	Two-way repeated measures ANOVA	1.0000000
ff	Normal	Two-way repeated measures ANOVA	0.1898718
gg [Fig. 8F, contra]	Normal	Two-way repeated measures ANOVA	1.0000000

Table 3